Global Biogeochemical Cycles

RESEARCH ARTICLE
10.1029/2019GB006348

A Global Model for Methylmercury Formation and Uptake at the Base of Marine Food Webs

Yanxu Zhang[1,2], **Anne L. Soerensen**[2,3,4], **Amina T. Schartup**[2,3,5], and **Elsie M. Sunderland**[2,3]

[1]Joint International Research Laboratory of Atmospheric and Earth System Sciences, School of Atmospheric Sciences, Nanjing University, Nanjing, China, [2]Harvard John A. Paulson School of Engineering & Applied Sciences, Harvard University, Cambridge, MA, USA, [3]Department of Environmental Health, Harvard T. H. Chan School of Public Health, Harvard University, Boston, MA, USA, [4]Department of Environmental Science and Analytical Chemistry, Stockholm University, Stockholm, Sweden, [5]Scripps Institution of Oceanography, La Jolla, CA, USA

Abstract Monomethylmercury (CH_3Hg) is the only form of mercury (Hg) known to biomagnify in food webs. Here we investigate factors driving methylated mercury [MeHg = CH_3Hg + $(CH_3)_2Hg$] production and degradation across the global ocean and uptake and trophic transfer at the base of marine food webs. We develop a new global 3-D simulation of MeHg in seawater and phyto/zooplankton within the Massachusetts Institute of Technology general circulation model. We find that high modeled MeHg concentrations in polar regions are driven by reduced demethylation due to lower solar radiation and colder temperatures. In the eastern tropical subsurface waters of the Atlantic and Pacific Oceans, the model results suggest that high MeHg concentrations are associated with enhanced microbial activity and atmospheric inputs of inorganic Hg. Global budget analysis indicates that upward advection/diffusion from subsurface ocean provides 17% of MeHg in the surface ocean. Modeled open ocean phytoplankton concentrations are relatively uniform because lowest modeled seawater MeHg concentrations occur in oligotrophic regions with the smallest size classes of phytoplankton, with relatively high uptake of MeHg and vice versa. Diatoms and synechococcus are the two most important phytoplankton categories for transferring MeHg from seawater to herbivorous zooplankton, contributing 35% and 25%, respectively. Modeled ratios of MeHg concentrations between herbivorous zooplankton and phytoplankton are 0.74–0.78 for picoplankton (i.e., no biomagnification) and 2.6–4.5 for eukaryotic phytoplankton. The spatial distribution of the trophic magnification factor is largely determined by the zooplankton concentrations. Changing ocean biogeochemistry resulting from climate change is expected to have a significant impact on marine MeHg formation and bioaccumulation.

Key Points:
- A new global ocean model for methylmercury formation and plankton food web dynamics is developed
- Important drivers are identified: substrate availability, microbial activity, shortwave radiation, community structure, and temperature
- The model developed in this study provides a quantitative framework for evaluation of the impact of climate change

Supporting Information:
- Supporting Information S1

Correspondence to:
Y. Zhang,
zhangyx@nju.edu.cn

Citation:
Zhang, Y., Soerensen, A. L., Schartup, A. T., & Sunderland, E. M. (2020). A global model for methylmercury formation and uptake at the base of marine food webs. *Global Biogeochemical Cycles*, *34*, e2019GB006348. https://doi.org/10.1029/2019GB006348

Received 29 JUN 2019
Accepted 26 JAN 2020
Accepted article online 3 FEB 2020

1. Introduction

Exposure to the neurotoxicant, monomethylmercury (CH_3Hg), in the USA and many other countries is predominantly from consumption of marine fish (Mahaffey et al., 2011; Sunderland et al., 2018). In seawater, there are two forms of methylated mercury (MeHg) species commonly measured in acidified samples: CH_3Hg and dimethylmercury [$(CH_3)_2Hg$]. CH_3Hg is the only form of mercury (Hg) that biomagnifies in food webs. It is formed biotically when microbes add a methyl group to inorganic divalent Hg (Hg^{II}) (Fitzgerald et al., 2007). Atmospheric deposition of inorganic Hg is the main source to the ocean (Amos et al., 2013; Sunderland & Mason, 2007), and concentrations have been enriched by the cumulative history of anthropogenic emissions (Horowitz et al., 2014; Streets et al., 2017). Many studies have reported enrichment of MeHg in some regions of the marine water column (Mason et al., 2012 and references therein). However, biogeochemical controls on spatial variability in MeHg production, degradation, and bioavailability are still poorly understood. Here we develop and evaluate a new global simulation for seawater MeHg concentrations and uptake at the base of the marine food web.

A major advance in the understanding of MeHg formation was enabled by identification of a two-gene cluster (hgcAB) in microorganisms responsible for methylation that is present in diverse environments (Parks et al., 2013). However, most organisms with the hgcAB gene cluster are from anoxic environments, which are rare in seawater samples from the open ocean (Bowman et al., 2019; Podar et al.,

2015). Incubations of Hg stable isotopes have shown that active production of MeHg from Hg^{II} occurs both in coastal and in shelf sediments (Hammerschmidt et al., 2004; Hollweg et al., 2009; Sunderland et al., 2004) and the marine water column (Lehnherr et al., 2011; Monperrus et al., 2007; Munson et al., 2018; Schartup et al., 2015). High concentrations of MeHg have been reported in subsurface marine waters (approximately 200–500 m) at different regions as well as near hydrothermal vents (Bowman et al., 2015, 2016; Bratkič et al., 2016; Canário et al., 2017; Cossa et al., 2011; Hammerschmidt & Bowman, 2012; Kim et al., 2017; Lamborg et al., 2016; Munson et al., 2015; Sunderland et al., 2009). A variety of studies have suggested that coastal sediment is responsible for the majority of MeHg in pelagic fisheries (Hammerschmidt & Fitzgerald, 2006), but more recent global estimates suggest that active production in the marine water column is a larger source to open ocean regions (Mason et al., 2012; Semeniuk & Dastoor, 2017; Soerensen et al., 2016).

Sunderland et al. (2009) found a significant and linear relationship between MeHg concentration and rates of organic carbon remineralization (OCRR) throughout the subsurface North Pacific Ocean. The authors suggested that heterotrophic bacterial activity, indicated by organic carbon remineralization, might therefore provide a reasonable proxy for MeHg production potential of different regions of the ocean. Many other studies have similarly found strong relationships between seawater MeHg concentrations, nutrients, and dissolved oxygen that also covary with turnover of organic carbon in the marine water column (Bowman et al., 2016; Cossa et al., 2009, 2011; Kim et al., 2017; Kirk et al., 2008; Lehnherr et al., 2011). Other studies did not find significant correlations between MeHg and these parameters (Agather et al., 2019; Bowman et al., 2015; Heimburger et al., 2015; Munson et al., 2015). This suggests that a myriad of factors influence the production, degradation, and transport of MeHg and thereby eventually its distribution in the seawater columns. Here we use these combined data from the world's oceans to constrain MeHg production.

Prior work has identified the occurrence of both photochemical and biological degradations of MeHg (DiMento & Mason, 2017; Black et al., 2012; Monperrus et al., 2007). Laboratory studies suggest that the photodegradation rate for MeHg in seawater depends on local incident photon intensity and light attenuation by chlorophyll, dissolved organic matter, and total suspended materials (DiMento & Mason, 2017; Lehnherr et al., 2011; Monperrus et al., 2007; Whalin et al., 2007). Below the photic layer, biotic and other abiotic processes (e.g., reactions with OH radicals) will dominate (Monperrus et al., 2007; Whalin et al., 2007). Previous studies have found two major microbial demethylation mechanisms: reductive or oxidative, dependent on the oxidation state of the carbon product evolved from the methyl group (CH_4 or CO_2) (Fitzgerald et al., 2007). Rates of Hg^{II} methylation and MeHg demethylation have been measured in seawater using enriched stable Hg isotope incubations (Lehnherr et al., 2011; Munson et al., 2018; Schartup, Balcom, et al., 2015; Soerensen et al., 2018). Demethylation is inhibited by low temperatures (Heyes et al., 2006; Mason & Fitzgerald, 1993; Mason & Sullivan, 1999; Matilainen & Verta, 1995).

MeHg present in seawater enters the marine food web mainly by passive diffusion across the cell of marine phytoplankton (Kim et al., 2014; Lee & Fisher, 2016). Algae are consumed by zooplankton, which results in a biomagnification of MeHg in seawater by up to 10,000 times (Schartup et al., 2018). Laboratory studies with multiple marine phytoplankton species have demonstrated that cell surface area to volume ratios provide a good proxy for uptake of MeHg (Kim et al., 2014; Lee & Fisher, 2016). Schartup et al. (2015) showed that terrestrial dissolved organic carbon (DOC) strongly affects the bioavailability of seawater MeHg. Schartup et al. (2018) developed a process-based model for MeHg uptake by phytoplankton and subsequent dietary transfer to zooplankton and applied it in several marine ecosystems in the northwest Atlantic margin. Here we extend the parameterization to the world's oceans.

The main objective of this work is to investigate the biogeochemical factors driving MeHg production, degradation, and food web uptake across the global ocean. We develop a new global 3-D simulation of MeHg concentrations in seawater and plankton using experimental data on MeHg production and degradation rates. We evaluate the model by synthesizing available seawater and plankton MeHg concentration data and comparing them to model results. Results are used to develop global budgets for MeHg in seawater and plankton. We quantify the relative importance of particle settling, ocean transport, and in situ methylation/demethylation for biological MeHg concentrations and discuss implications for future climate-driven changes in ocean biogeochemistry.

2. Materials and Methods

2.1. General Model Description

We developed a new simulation for MeHg chemistry, transport, and trophic transfer within the Massachusetts Institute of Technology general circulation model (MITgcm) (Marshall et al., 1997). The model is configured following the baseline solution for the nonlinear inverse modeling framework ECCO v4, which provides an estimate for the evolving ocean state between 1992 and 2011 (Forget et al., 2015). The model has a resolution of 1° × 1° horizontally and 50 vertical levels and is run with a time step of 60 min. The resolution is higher near the equator (0.5° latitude × 1° longitude) and the Arctic (approximately 40 × 40 km).

This model builds on the MITgcm simulation for inorganic Hg species by Zhang et al. (2015) that simulates the photochemical and biological transformations between aqueous elemental (Hg^0) and Hg^{II}, the partitioning of Hg^{II} onto particulate organic carbon (POC) to form Hg^P, and the sinking of Hg^P to deeper waters. This POC pool includes both detritus and living phytoplankton, as partitioning of inorganic Hg^{II} to living and dead cells is similar (Pickhardt & Fisher, 2007). The model also simulates exchange of Hg^0 with the atmosphere and is forced by atmospheric Hg^{II} deposition and Hg^0 concentrations in the marine boundary layer from the Goddard Earth Observing System-Chem global atmospheric Hg simulation (Horowitz et al., 2017). The model is initialized with the present-day (2008) Hg concentrations from the offline global 3-D ocean tracer model [*Zhang et al.,* 2014]. The model is run for 10 years, and the result of the last year simulation is used for analysis.

We use a coupled ocean plankton ecology and biogeochemistry model (the Darwin project; http://darwinproject.mit.edu) within the MITgcm to simulate production and growth of different plankton species, suspended particulate matter concentrations, and organic carbon remineralization in the marine water column. This model simulates the cycling of nutrients (C, N, P, Si, and Fe), phytoplankton growth, zooplankton grazing, and mortality (Dutkiewicz et al., 2009; Ward et al., 2013; Zhang et al., 2015). We extract six categories of phytoplankton with different sizes, growth rates, affinity to nutrients, and other physiological parameters. They include three larger eukaryotic groups, diatoms (fast growing and using silica, diameter = 12 μm), coccolithophores (with calcium carbonate plates, 5 μm), and other large taxa such as dinoflagellates (fast growing but not using silica, 10 μm); two picocyanobacteria, prochlorococcus (not using NO_3 and low equilibrium resource concentrations, 0.6 μm) and synechococcus (low equilibrium resource concentrations, 1.8 μm); and trichodesmium (a diazotroph, 10 μm) (Supporting Information Figure S1).

The Darwin model includes two categories of herbivorous zooplankton (small [30 μm] and large [300 μm]) with different dietary preference among the six phytoplankton groups. We archive the monthly concentrations of chlorophyll, DOC, and POC and the biomass of all plankton species (carbon content) to capture seasonal variability. We also archive the monthly average net primary production (NPP), OCRR fluxes, sinking fluxes for POC and large phytoplankton, and zooplankton grazing and mortality rates. These parameters are then used to scale the partitioning of Hg between seawater and particles, transformation rates among different Hg species, and uptake and trophic transfer by marine plankton.

2.2. Formation and Degradation of MeHg

We added CH_3Hg and $(CH_3)_2Hg$ as tracers to the Hg species simulation within the MITgcm (Figure 1). Reaction rates for formation and degradation are based on experimentally measured values from Lehnherr et al. (2011), which differentiates the methylation rates from Hg^{II} to CH_3Hg and CH_3Hg to $(CH_3)_2Hg$. Experimental rates vary among regions as a function of environmental conditions (e.g., Lehnherr et al., 2011 ; Munson et al., 2018 ; Schartup, Balcom, et al., 2015 ; Soerensen et al., 2018). We therefore scale measured reaction rates in the model based on environmental parameters (e.g., OCRR, solar radiation intensity, and temperature). We include methylation from Hg^{II} to CH_3Hg (k_{m1}) and from CH_3Hg to $(CH_3)_2Hg$ (k_{m2}), as well as photochemical demethylation of CH_3Hg to Hg^{II} (k_{dm1}) and $(CH_3)_2Hg$ to CH_3Hg (k_{dm2}). The methylation rates (k_{m1} and k_{m2}) are scaled proportionally to OCRR as suggested by Sunderland et al. (2009) (Table 1). Photochemical demethylation (k_{dm1} and k_{dm2}) is scaled by the intensity of shortwave radiation (hv) attenuated by seawater pigments (chlorophyll and DOC) (Table 1). The dark (biotic or abiotic) demethylation rate (k_{dm3}) is parameterized to be temperature (T) dependent

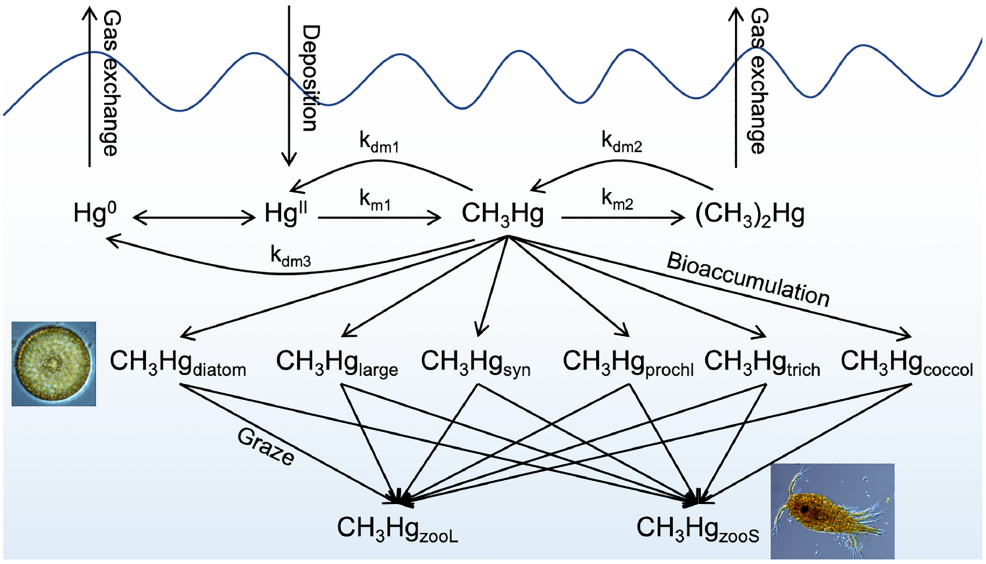

Figure 1. Schematic representation of MeHg biogeochemistry and food web dynamics in the global ocean. Hg^0 and Hg^{II} represent the elemental and divalent inorganic mercury pools, respectively, and CH_3Hg and $(CH_3)_2Hg$ are for monomethylmercury and dimethylmercury, respectively. CH_3Hg in the six types of phytoplankton are denoted as CH_3Hg_{diatom}, CH_3Hg_{large}, CH_3Hg_{prochl}, CH_3Hg_{syn}, CH_3Hg_{trich}, and CH_3Hg_{coccol}, which represent diatoms (12 μm), other large phytoplankton (10 μm), prochlorococcus (0.6 μm), synechococcus (1.8 μm), trichodesmium (10 μm), and coccolithophores (5 μm), respectively (Dutkiewicz et al., 2009). CH_3Hg_{zooL} and CH_3Hg_{zooS} are for CH_3Hg in large (300 μm) and small herbivorous (30 μm) zooplankton, respectively. The arrows among Hg species represent their biogeochemical transformations in seawater. The arrows between seawater MeHg and phytoplankton represent uptake and those between phytoplankton and zooplankton indicate trophic transfer.

(Matilainen & Verta, 1995) (Table 1). Direct methylation of Hg^{II} to $(CH_3)_2Hg$ is neglected because of its extremely slow reaction rate (Lehnherr et al., 2011).

We model concentrations of particulate CH_3Hg (CH_3Hg^P, mol m^{-3}) in seawater based on a partition coefficient (K_d) with dissolved phase CH_3Hg concentrations (mol m^{-3}), POC, and the fraction of organic carbon in suspended particulate matter (f_{oc}) (Table 1). Pickhardt and Fisher (2007) found CH_3Hg partitions differently between living and dead cells. We therefore exclude the living phytoplankton for the POC pool when parameterizing partitioning of CH_3Hg to suspended particles. The model representation of uptake of CH_3Hg by living cells (phytoplankton) is described in section 2.3. Sinking of CH_3Hg^P is calculated based on export flux curves for POC as a function of depth in the marine water column, following Zhang et al. (2014). Air–sea exchange of $(CH_3)_2Hg$ is calculated based on the open seawater surface area, piston velocity, and the concentration gradient across the air–sea interface (Nightingale et al., 2000), with a constant atmospheric $(CH_3)_2Hg$ concentration (4 pg m^{-3}) (Soerensen et al., 2016).

2.3. Uptake of MeHg by Plankton and Trophic Transfer to Zooplankton

The uptake of CH_3Hg in seawater by phytoplankton is modeled as an instantaneous equilibrium process because the time to steady state has been shown to be on the order of hours (Kim et al., 2014). The volume concentration factor (VCF, the ratio of CH_3Hg concentration in phytoplankton [CH_3Hg_{phy}] over the seawater concentration) is a function of the cell diameter (d) and DOC concentrations following Schartup et al. (2018) (Table 1). Redistribution of CH_3Hg between seawater and phytoplankton is calculated for each model time step after the partitioning between seawater and POC.

Trophic transfer of CH_3Hg from phytoplankton to zooplankton ($F_{graze}^{CH_3Hg}$) is calculated after phytoplankton uptake based on the biomass of phytoplankton grazed by zooplankton (F_{graze}^{Carbon}), the biomass concentration of phytoplankton (Phy), and the assimilation efficiency of zooplankton (A_{ED}) (Schartup et al., 2018) (Table 1). Unassimilated CH_3Hg grazed by zooplankton returns to the seawater in the form of CH_3Hg^P.

Table 1
Model Parameterization for CH_3Hg and $(CH_3)_2Hg$ Formation/Degradation, food Web Uptake and Trophic Transfer

Parameter	Units	Description	Equation or value
k_{m1}	s^{-1}	Methylation rate from inorganic Hg^{II} to CH_3Hg [a]	$4.4 \times 10^{-7} \times$ OCRR
k_{m2}	s^{-1}	Methylation rate from CH_3Hg to $(CH_3)_2Hg$ [a]	9.3×10^{-9}
k_{dm1}	s^{-1}	Demethylation rate from CH_3Hg to Hg^{II} [a]	$8.0 \times 10^{-8} \times hv$
k_{dm2}	s^{-1}	Demethylation rate from $(CH_3)_2Hg$ to CH_3Hg [a]	$1.9 \times 10^{-8} + 3.8 \times 10^{-9} \times hv$
k_{dm3}	s^{-1}	Demethylation rate from CH_3Hg to Hg^0	$1.1\times10^{-8}\times\exp\left(-5500\times\left(\frac{1}{T}-\frac{1}{293.15}\right)\right)$
k_{elim}	s^{-1}	Elimination rate of CH_3Hg from zooplankton [b]	$3.8 \times 10^{-8} \times {M_{zoo}}^{-0.195} \times e^{0.0066T}$
k_d	$L\ kg^{-1}$	Partition coefficient of CH_3Hg between seawater and POC [a]	6.3×10^3
f_{oc}	Unitless	Fraction of organic carbon in suspended particulate matter [a]	10%
1. VCF	Unitless	Volume concentration factor of CH_3Hg between phytoplankton and seawater [b]	$2.8\times10^6\times\frac{1}{d}\times e^{-0.008\cdot DOC}$
d	μm	Plankton cell diameter [c]	Diatoms: 12 μm coccolithophores: 5 μm other large: 10 μm prochlorococcus: 0.6 μm synechococcus: 1.8 μm trichodesmium: 10 μm small zooplankton: 30 μm large zooplankton: 300 μm
2. DOC	μM	Dissolved organic carbon concentration in seawater [d]	Darwin model output
3. POC	$kg\ L^{-1}$	Particulate organic carbon concentration in seawater	Darwin model output
4. OCRR	$mmol\ m^{-3}\ day^{-1}$	Organic carbon remineralization rate	Darwin model output
hv	$W\ m^{-2}$	Incoming shortwave radiation flux	Darwin model output
T	K	Seawater temperature	Darwin model output
5. A_{ED}	Unitless	Assimilation efficiency of zooplankton for CH_3Hg [b]	0.6
6. CH_3Hg	$mol\ m^{-3}$	CH_3Hg concentrations in dissolved phase	Model tracer
7. $(CH_3)_2Hg$	$mol\ m^{-3}$	$(CH_3)_2Hg$ concentrations in dissolved phase	Model tracer
8. CH_3Hg^P	$mol\ m^{-3}$	Particulate CH_3Hg concentrations [a]	Model tracer, and $\frac{[CH_3Hg^P]}{[CH_3Hg]} = \frac{K_d}{f_{oc}} \times [POC]$
$F_{graze}^{CH_3Hg}\big\vert_{i,j}$	$mol\ m^{-3}\ s^{-1}$	The transfer rate of CH_3Hg from ith phytoplankton to jth zooplankton via dietary uptake	$A_{ED} \times F_{graze}^{Carbon}\big\vert_{i,j} \times \frac{CH_3Hg^i_{phy}}{Phy_i}$
$F_{mortality}^{CH_3Hg}\big\vert_j$	$mol\ m^{-3}\ s^{-1}$	The flux of CH_3Hg that is released back to seawater from the jth zooplankton due to mortality	$F_{mortality}^{Carbon}\big\vert_j \times \frac{Ch_3Hg^j_{zoo}}{Zoo_j}$
F_{graze}^{Carbon}	$mol\ m^{-3}\ s^{-1}$	Biomass (in carbon content) of phytoplankton grazed by zooplankton	Darwin model output
$F_{mortality}^{Carbon}$	$mol\ m^{-3}\ s^{-1}$	Rate of carbon release to seawater following zooplankton mortality	Darwin model output
9. CH_3Hg_{phy}	$mol\ m^{-3}$	CH_3Hg concentrations in phytoplankton	Model tracer
10. CH_3Hg_{zoo}	$mol\ m^{-3}$	CH_3Hg concentrations in zooplankton	Model tracer
11. Phy	$mol\ m^{-3}$	Biomass (in carbon content) concentration of phytoplankton	Darwin model output
12. Zoo	$mol\ m^{-3}$	Biomass (in carbon content) concentration of zooplankton	Darwin model output
13. M_{zoo}	g	Wet weight of zooplankton cell	$V\rho$
V	μm^3	Volume of cell	$\frac{1}{6}\pi {d_j}^3$
ρ	$g\ cm^{-3}$	Density of zooplankton [b]	1.0

Note. The parameterization for the redox reactions between Hg^0 and Hg^{II}, partitioning between Hg^{II} and Hg^P, Hg^P sinking, and $(CH_3)_2Hg$ air–sea exchange are available in *Zhang et al.* (2014, Zhang et al., 2015) and Soerensen et al. (2016).
Abbreviations: DOC, dissolved organic carbon; OCRR, rates of organic carbon remineralization; POC, particulate organic carbon; VCF, volume concentration factor.
[a]Soerensen et al., 2016. [b]Schartup et al., 2018. [c]Dutkiewicz et al., 2009. [d]Hansell et al., 2009.

The total mass of CH_3Hg in the zooplankton cells is increased by grazing. Losses reflect CH_3Hg elimination through fecal excretion and mortality. The flux of CH_3Hg that is released back to seawater from zooplankton due to mortality ($F_{mortality}^{CH_3Hg}$) is calculated based on the rate of remineralized carbon released to seawater from zooplankton following mortality (F_{graze}^{Carbon}), the CH_3Hg concentrations in zooplankton (CH_3Hg_{zoo}), and the zooplankton biomass (zoo). The elimination of CH_3Hg from zooplankton is modeled as a first-order

Table 2
Summary of Cruise Data Used for Model Evaluation in This Study

Cruise	Region	Time	Depth	Sample Size	Total Hg (pM) Depth < 150 m	Total Hg (pM) Depth > 150 m	MeHg (fM) Depth < 150 m	MeHg (fM) Depth > 150 m
RITS[a]	Equatorial Pacific	Jan–Feb 1990	Top 900 m	59	3.1 ± 2.5	4.0 ± 2.0	98 ± 120	310 ± 260
P16N[b]	North Pacific	Mar 2006	Top 1000 m	80	0.99 ± 0.32	1.4 ± 0.37	95 ± 52	260 ± 110
SR3[c]	Southern Ocean	Mar–Apr 2008	Whole column	285	1.0 ± 0.72	1.1 ± 0.47	150 ± 120	430 ± 190
GA03[d]	North Atlantic	Oct–Nov 2010; Nov–Dec 2011	Whole column	706	0.77 ± 0.41	0.99 ± 0.62	77 ± 90	130 ± 140
Metzyme[e]	Central tropical Pacific	Oct 2011	Whole column	233	0.30 ± 0.24	1.0 ± 0.34	31 ± 30	89 ± 47
SHIPPO[f]	Western Pacific	Jul 2012; Apr 2014	Top 500 m	174	0.82 ± 0.37	1.3 ± 0.47	27 ± 36	390 ± 270
ARK_XXVI_3[g]	Arctic	Aug–Sep 2011	Whole column	83	1.5 ± 1.4	0.83 ± 0.31	105 ± 108	132 ± 105
GP16[h]	Equatorial and South Pacific	Oct–Dec 2013	Whole column	692	0.44 ± 0.82	1.0 ± 0.44	64 ± 69	129 ± 99

[a]Mason and Fitzgerald (1993). [b]Sunderland et al. (2009). [c]Cossa et al. (2011). [d]Bowman et al. (2015). [e]Munson et al. (2015). [f]Kim et al. (2017). [g]Heimburger et al. (2015). [h]Bowman et al. (2016).

process with constant k_{elim} calculated following Schartup et al. (2018) (Table 1). Note that the Darwin model tracks total mass of CH_3Hg in plankton cells in a unit volume of seawater (i.e., CH_3Hg mass per unit plankton biomass × plankton biomass per unit volume of seawater). The size of phytoplankton and zooplankton cells are fixed without considering the growth of individual cells, as well as the size and age distribution of individuals among their populations.

2.4. Model Evaluation Data

We synthesize available data in the literature for model evaluation (Table 2). Observations over the shelf and slope regions are excluded because they reflect regional variability in coastal and riverine inputs not captured by the resolution of the MITgcm (e.g., Fu et al., 2010). The main focus of this study is the global open ocean, where the riverine impact is significantly smaller than in the coastal regions (Zhang et al., 2015).

3. Results and Discussion

3.1. MeHg distribution

Figure 2a shows modeled and observed MeHg concentrations in the surface ocean (0–100 m). Observed MeHg concentrations are generally low in the top 100 m of the water column (<200 fM; 1fM = 10^{-15} mol/L). Higher concentrations (200–400 fM) are observed in high latitude regions such as the Canadian Archipelago and the Southern Ocean (Cossa et al., 2011; Kirk et al., 2008). The lowest concentrations (<50 fM) are observed in the midlatitude and low-latitude regions. For example, concentrations of ~10 fM have been reported over the midlatitude and low-latitude Pacific Ocean (SHIPPO, Metzyme, and GP16) (Bowman et al., 2016; Kim et al., 2017; Munson et al., 2015). Slightly higher concentrations are observed in the midlatitude and low-latitude North Atlantic Ocean (GA03) (Bowman et al., 2015). One exception is the higher concentrations (~50 fM) observed over the equatorial Pacific Ocean (Metzyme) and eastern tropical Pacific Ocean (GP16). Surface MeHg concentrations are higher (range = 26 to 139 fM) in the North Pacific Ocean (P16N). However, the detection limit for MeHg in samples collected on this cruise was 50 fM (Sunderland et al., 2009). Overall, the model reasonably captures the observed latitudinal pattern reasonably well with an average concentration of 43 ± 52 fM compared to 69 ± 67 fM for observations. The low model bias in surface waters compared to observations likely reflects an artifact in the observations associated with relatively high detection limits for total MeHg in some studies.

Figures 2b and 2c show the modeled subsurface MeHg concentrations at the subthermocline (500 m) and the permanent thermocline (1,000 m). Figure 3 also shows cross-sectional plots of MeHg concentrations in the top 1,000 m of the water column (or the maximum depth of cruises, whichever is smaller) along the cruises summarized in Table 2 for the Atlantic, Pacific, and Southern Oceans, respectively. In this figure, multiple

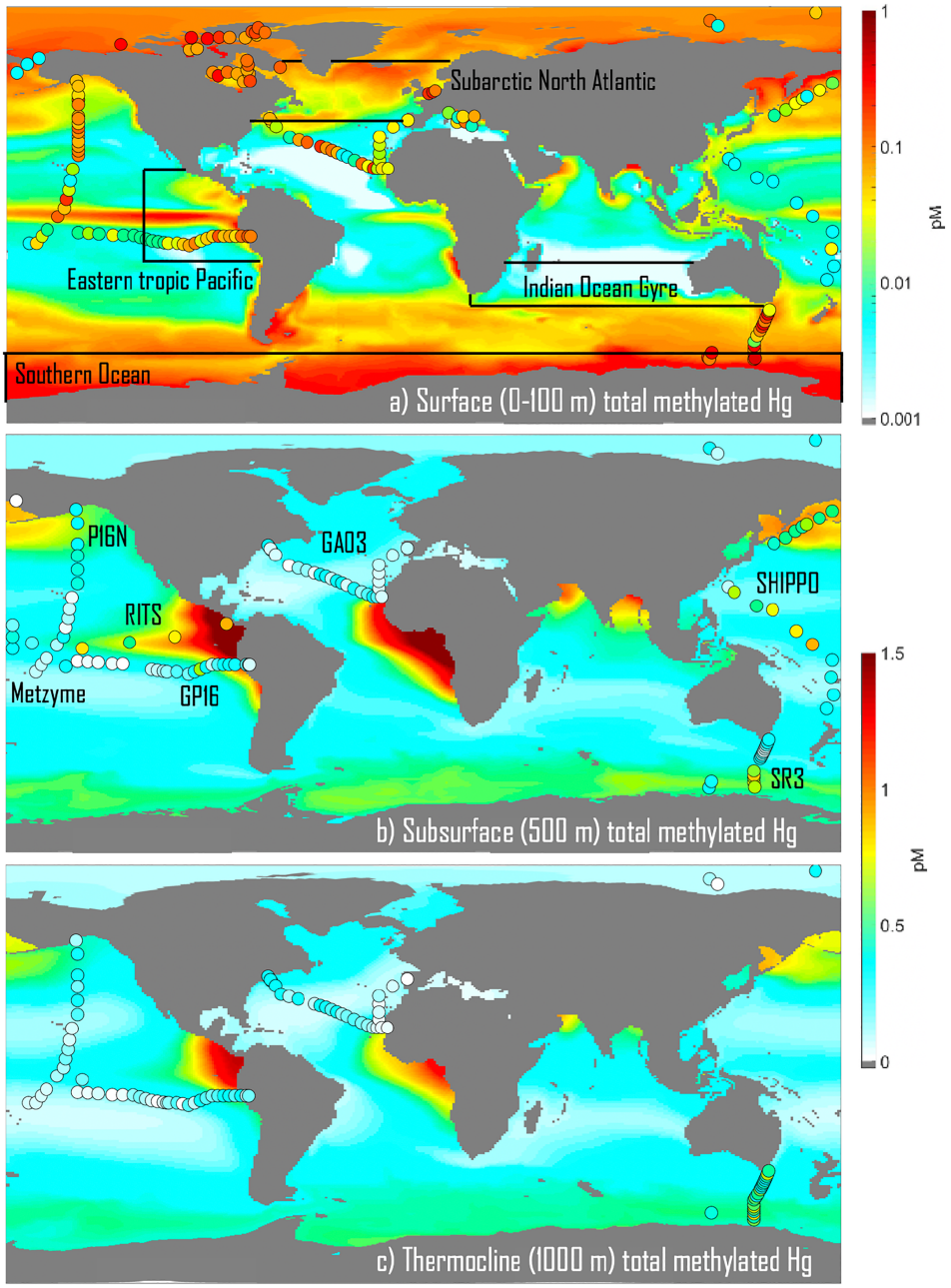

Figure 2. Modeled annual mean MeHg concentrations in seawater at depths (a) 0–100 m, (b) 500 m, and (c) 1,000 m. The background color shows annual mean modeled values. Circles show available observations between 1990 and 2014. Labels on panels (a) and (b) are for different regions (used for model evaluation and budgets) and cruises, respectively. *Note*. the color scale for the surface ocean is on the log scale.

observed profiles (denoted by *n* in Figure 3) with similar concentration patterns are also plotted together against the average model profiles at the same locations.

Subsurface MeHg concentrations show different patterns compared with those of the surface ocean. As seen in Figure 2b, significantly higher concentrations are observed at 500-m depth in the eastern tropical Pacific (Figure 3d; RITS, ~700 fM), high latitude Pacific (Figure 3e; SHIPPO, 400–500 fM), and the Southern Ocean (Figure 3f; SR3, approximately 400–600 fM). The concentrations are much lower over the North Atlantic Ocean (Figures 3a and 3b; GA03, 100–200 fM) and at the center of the tropical Pacific Ocean (Figure 3c; Metzyme, 40–200 fM). The model captures these spatial patterns relatively well ($r = 0.48$), and there is no

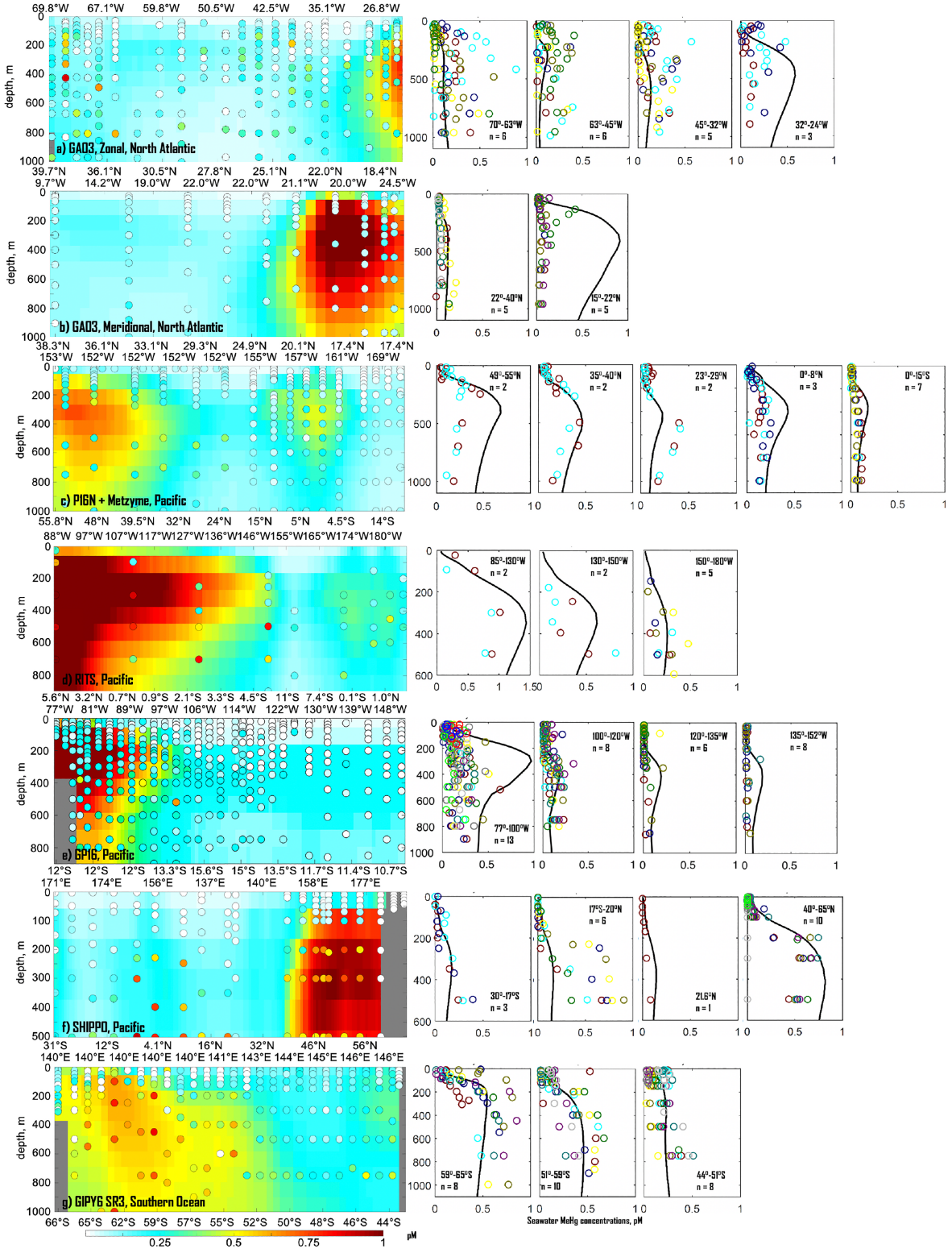

Figure 3. Comparison of modeled seawater MeHg concentrations and cross sections and vertical profiles from various cruises. Panels (a) and (b) show cruise track GA03 (zonal and meridional transects, respectively) (Bowman et al., 2015), panel (c) shows the P16N + Metzyme cruises (Munson et al., 2015; Sunderland et al., 2009), (d) RITS (Mason & Fitzgerald, 1993), (e) GP16 (Bowman et al., 2016), (f) SHIPPO (Kim et al., 2017), and (g) GIPY6 SR3 (Cossa et al., 2011). The background colors in the left panel columns represent annual mean modeled MeHg concentrations, and observations are shown as circles. For the right column panels, black lines show the annual mean modeled MeHg concentration, and circles represent observations. Figure 2 shows corresponding cruise tracks for observations presented here.

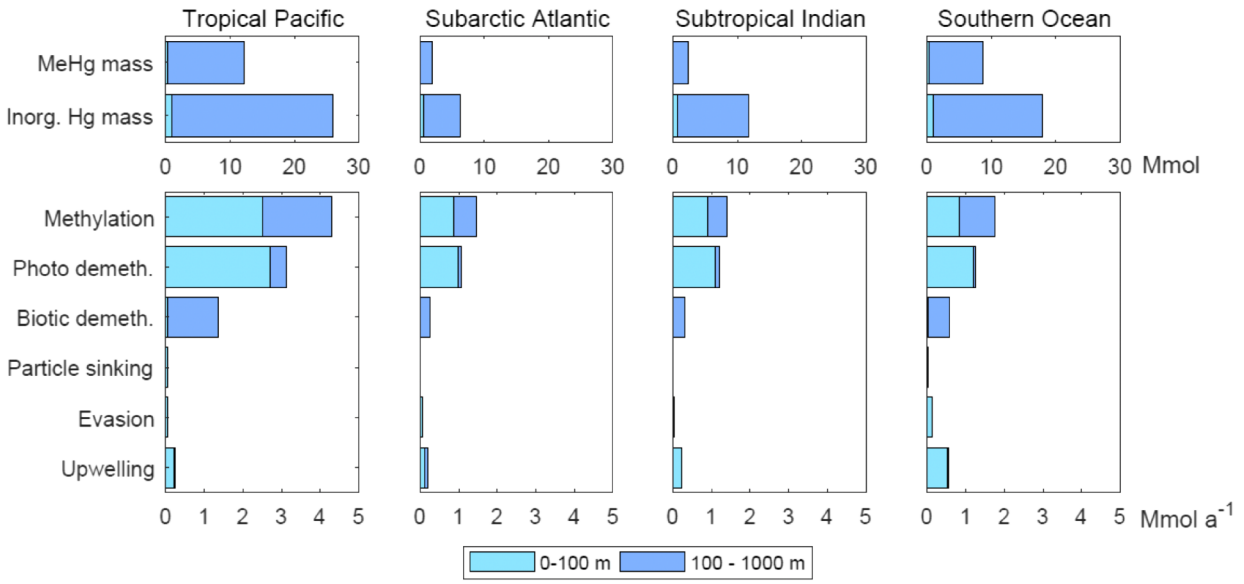

Figure 4. Mass budget for MeHg (including also the mass of inorganic Hg) in four regions: eastern tropical Pacific (20°S–20°N, east of 120°W), subarctic Atlantic (north of 40°N), subtropical Indian (20°S–40°S), and Southern Ocean (south of 60°S), as shown in Figure 2. Inorganic Hg includes all inorganic Hg species in the dissolved and particulate phases, and MeHg includes CH_3Hg and $(CH_3)_2Hg$ in the dissolved and particulate phases as well as in plankton. The surface (0–100 m) and subsurface (100–1,000 m) mass/mass flows are indicated by different colors on the plot. Particle sinking and upwelling fluxes are shown for 100 m for the surface ocean and 1,000 m for the subsurface ocean.

significant difference between modeled (360 ± 280 fM) and observed values (340 ± 260 fM) (*t* test, $p = 0.96$). The model predicts that highest MeHg concentrations extend to ~25° north and south over the eastern tropical Pacific and Atlantic Oceans off the Central/South American and African continents. This corresponds to the enhanced primary production and microbial activity over these major ocean upwelling zones along the edge of the eastern boundary currents. This prediction agrees well with the RITS (Figure 3d). However, the model overestimates the observations east of 120°W of the GP16 cruise (observation = ~200 fM vs. model = ~600 fM) and south of 20°N of GA03 cruises (observation = ~100 fM vs. model = ~600 fM), which are at the edges of the modeled high concentration regions (Figure 2b). This may reflect different sampling season and the strength of upwelling during these studies and/or the model uncertainty in representing the spatial extent of these biologically active regions. The model also predicts high MeHg concentrations over other upwelling regions such as the tropical Arabian Sea and Bay of Bengal (750–1,000 fM). The model values over midlatitude regions, especially over the center of gyres, are generally <200 fM, consistent with the observations (Figure 2b).

Observed MeHg concentrations at 1,000-m depth (Figure 2c) are lower than those at 500 m but with very similar spatial patterns. This reflects the influence of MeHg production that is associated with primary production and microbial activity. The model successfully reproduces the observed spatial pattern ($r = 0.56$), and there is no significant difference between modeled (260 ± 170 fM) and observed values (290 ± 210 fM) (paired *t* test, $p = 0.93$).

3.2. Controlling Factors

We compare the MeHg mass budgets for four typical regions of the global ocean (Figure 4): (a) the eastern tropic Pacific (representing tropical regions with active microbial activity); (b) the Southern Ocean (cold polar environment); (c) the Indian Ocean Gyre (downwelling and oligotrophic environments); and (d) the subarctic North Atlantic Ocean (deep-water formation regions) (boundaries for different regions are shown in Figure 2a). These regions represent a diverse range of factors affecting MeHg production and degradation such as microbial activity, atmospheric deposition, and temperature. Contrasting budgets from different regions provide insights into the major factors affecting MeHg formation and distribution.

3.2.1. Substrate Availability

Inorganic Hg^{II} species provide the substrate for methylation and are an important controlling factor for the distribution of MeHg. In the surface ocean and subthermocline (~500-m depth), Hg^{II} concentrations respond to atmospheric inputs over a time scale of several decades in most ocean regions and are strongly influenced by the magnitude of atmospheric dry/wet deposition (Zhang, Jaeglé, & Thompson, 2014). The association between enhanced atmospheric Hg deposition over the intertropical convergence zone and elevated seawater Hg concentrations has been observed by Kuss et al. (2011), Soerensen et al. (2014), and Zhang et al. (2019). Elevated concentrations of oxidants for Hg^0 (including Br, HO_2, and NO_2) and high precipitation rates mean the tropical oceans (30°S–30°N) account for 49% of global Hg^{II} deposition (Horowitz et al., 2017). These high atmospheric inputs lead to higher seawater total Hg concentrations (~1.5 pM) and MeHg concentrations (500–700 fM) in the upper ~1,000 m of these regions, as observed on the RITS and SHIPPO cruises (Kim et al., 2017; Mason & Fitzgerald, 1993) and ALOHA station (*Motta* et al., *n.d.*). For instance, total Hg concentrations as high as 1.5 pM and MeHg concentrations up to 800 fM have been reported in the tropical part of the SHIPPO cruise (Kim et al., 2017). The RITS cruise study reported average total Hg concentrations up to 4.0 pM in the equatorial Pacific Ocean, but early sampling and analytical techniques may mean these values are less reliable than recent measurements.

Modeled seawater MeHg concentrations (1,300 ± 310 fM) in the upper 1,000 m of the eastern tropical Pacific Ocean (east of 145°W) are not significantly different from those measured on the RITS cruise (960 ± 60 fM, $p = 0.28$) (Mason & Fitzgerald, 1993). However, the model overestimates measurements from the GP16 cruise that is ~10–15° south of RITS cruise (model, 170 ± 276 fM; and observations, 110 ± 100 fM in the upper 1,000 m) (Bowman et al., 2016). The model also significantly underestimates the MeHg concentrations over the western tropical Pacific Ocean (17°S–20°N, covered by SHIPPO cruise; model, 130 ± 20 fM; and observation, 510 ± 290 fM in the upper ~500 m; $p = 0.043$), even though the model captures the total Hg concentrations over this region relatively well (model, 1.7 ± 0.16 pM; and observation, 1.5 ± 0.51 pM, $p = 0.71$) (Kim et al., 2017). These discrepancies, as discussed above, are associated with the model uncertainty in spatial distribution of ocean productivity. The model also cannot capture the fine-scale variability of observations associated with small-scale circulations and eddies due to the relatively coarse model resolution.

3.2.2. Microbial Activity

Another important factor controlling seawater MeHg concentrations is microbial activity. We use OCRR as an indicator for microbial activity as suggested by Sunderland et al. (2009). Regions with high productivity and thus relatively active microbial activity, such as the eastern tropical Pacific and Atlantic, and high-latitude North Pacific, all have higher MeHg concentrations (500–800 fM) in subsurface seawater compared to the midlatitude oligotrophic regions covered by the GA03 cruises (100–200 fM). The overlap between high Hg^{II} concentrations and active microbial activity results in the highest observed MeHg concentrations in the subsurface waters of the eastern tropical Pacific Ocean, which are well captured by the model. On the other hand, the model predicts relatively low MeHg concentrations (100–200 fM) in subsurface seawater for the central tropical Pacific Ocean due to oligotrophic conditions and thus low Hg^{II} methylation potential in these waters, even though atmospheric Hg inputs are similar or even higher than the eastern tropical Pacific Ocean, consistent with the observations from Metzyme, RITS, and GP16 cruises (Figures 2b and 3c–e). The model also predicts low MeHg concentrations across the upper 1,000 m of the North Atlantic Gyre (110 ± 17 fM), which is consistent with observations (124 ± 150 fM) ($p = 0.93$) (Figure 3a).

Observed MeHg concentrations (490 ± 210 fM) in the upper 500 m of the water column between 40° and 65°N on the SHIPPO cruise in the western North Pacific Ocean are approximately two times higher than between 49° and 55°N on the P16N cruise in the eastern North Pacific Ocean (230 ± 66 fM). Besides the regional difference between the eastern and western North Pacific Ocean, this may reflect different sampling seasons for the two cruises: July for SHIPPO and March for P16N (Table 2). Primary production in the Pacific is much higher in July than March; for example, approximately three times in the Pacific subarctic gyre (Matsumoto et al., 2014). Elevated primary production and microbial activity lead to higher MeHg concentrations over this region in the summer. Model results agree well with the SHIPPO cruise in this region (model, 690 ± 120 fM; $p = 0.41$; Figure 3e) but overestimate the P16N cruise by a factor of ~2 (model, 480 ± 90 fM; $p = 0.024$; Figure 3c). This is largely associated with the overestimate in primary production (similar for OCRR) by the Darwin model in the spring (Figure S2).

The average modeled Hg methylation rate (defined as the ratio of methylmercury production/mass of inorganic Hg^{II}) varies by a factor of ~2 over the global ocean. Highest rates (0.08–0.1 $year^{-1}$) are calculated over the subsurface eastern tropical Pacific Ocean and subarctic Atlantic, and lowest rate (~0.05 $year^{-1}$) are found in the Southern and subtropical Indian Oceans. This is consistent with the spatial distribution of satellite-derived NPP (http://www.science.oregonstate.edu/ocean.productivity). However, the modeled average MeHg concentrations are much higher over the tropical Pacific Ocean (540 fM) than the subarctic North Atlantic Ocean (220 fM). This is largely driven by the lower modeled inorganic Hg concentrations (~0.50 pM) over the North Atlantic compared to the tropical Pacific (0.88 pM).

3.2.3. Shortwave Radiation

We find that the observed MeHg concentrations in the surface ocean vary as a function of latitude (Figures 2a and S3a). The average MeHg concentration between 30°S and 30°N is 45 ± 48 fM, which is approximately a factor of 2 lower than polar regions (poleward of 60°, 110 ± 110 fM). This pattern is explained by variable photodemethylation rates (Figure S3b), which are proportional to shortwave radiation and a function of latitude. Methylation rates also influence concentrations in the surface ocean, but we find these are a secondary factor for ambient MeHg concentrations (Figure S3c). For instance, the modeled average methylation rate is $3.4 \times 10^{-3} \pm 1.8 \times 10^{-3}$ day^{-1} in polar regions, which is significantly lower than the other regions ($6.8 \times 10^{-3} \pm 5.6 \times 10^{-3}$ day^{-1}) despite having the highest MeHg concentrations. We conclude that variability in MeHg concentrations in the surface ocean mainly reflects degradation rates rather than formation.

Light penetration into the thermocline means photodemethylation is not limited to the top 100 m of all ocean regions. Depth dependence of light penetration is a function of seawater pigment concentrations that attenuate incident radiation (Wozniak & Dera, 2007) and also inhibit MeHg degradation. Lower pigment concentrations over oligotrophic ocean regions lead to greater light penetration, facilitating degradation of MeHg up to depths of ~250 m (Figure S4). This helps to explain the lowest observed MeHg concentrations in such regions. The midlatitude oligotrophic zone such as the center of the Indian Ocean Gyre has the fastest photochemical demethylation rate (0.10 day^{-1}) due to both relatively strong shortwave radiation and low pigment concentrations. The tropical Pacific Ocean and the subarctic Atlantic Ocean have average rates of 0.047 and 0.040 day^{-1}, respectively. The Arctic and Southern Oceans have the overall lowest rates (0.0082 and 0.013 day^{-1}, respectively) due to weaker solar radiation and elevated chlorophyll concentrations. These values are in the same range as those measured in prior work (0.003–0.43 day^{-1}) (Lehnherr et al., 2011; Monperrus et al., 2007; Whalin et al., 2007).

3.2.4. Particle Sinking

Sinking of suspended particles is a key mechanism for the transport of anthropogenic Hg into the subsurface ocean (e.g., Soerensen et al., 2010; Zhang et al., 2014). Our analysis suggests that for subsurface waters in the four selected regions, sinking of MeHg associated with suspended particles is a minor source term compared with in situ biological methylation (Figure 4), which is consistent with previous studies (Bowman et al., 2015; Kim et al., 2017). The ratio of the particulate sinking flux to the methylation flux at depths of 100 to 1,000 m ranges from 0.49% to 1.2%. This finding is also consistent with a previously derived budget for MeHg over the western Pacific Ocean (0.44–1.1%) (Kim et al., 2017). This is associated with the low MeHg concentrations in these particles (10^{-5}–10^{-4} fM by the model). However, Hg^{II} partitions more efficiently to suspended particles compared to MeHg species (Balcom et al., 2008). Particle sinking is an important mechanism delivering inorganic Hg^{II} species to subsurface waters, thus providing the substrate for MeHg formation. Larger K_d values for Hg^{II} and CH_3Hg compared to those used in the model were measured for water column samples (Lamborg et al., 2016; Bowman et al., 2016). However, a sensitivity run parameterizing the model with these K_d values results in unrealistic vertical profiles. Given the large uncertainties associated with the compositions and settling velocity of the suspended particles in the ocean, we optimized the K_d value to best reproduce observed vertical Hg^{II} and MeHg profiles.

3.2.5. Temperature

Degradation of MeHg via biotic/abiotic pathways is another important factor influencing MeHg concentrations, especially in the subsurface ocean. In the absence of light, biotic demethylation is the dominant degradation pathway for MeHg at seawater depths greater than 250 m. The sequential action of organomercurial lyase (MerB) and mercuric reductase (MerA) enzymes are thought to be associated with MeHg demethylation through the action of an Hg^{II}-responsive regulatory protein, MerR (Brown et al., 2003; Gionfriddo et al.,

2016). An inverse correlation between demethylation rates and Hg^{II} concentrations ranging from 10^{-1}–10^{4} pM has been identified in lake and sediment pore waters (Schaefer et al., 2004). However, microbes responsible for methylation may not be adapted to the low Hg^{II} concentrations typically observed in seawater since observed demethylation rates are usually very low (Schaefer et al., 2004). Matilainen and Verta (1995) found that demethylation of MeHg in surface waters is temperature dependent. We find that the dependence of demethylation rates on temperature is essential for explaining high observed MeHg concentrations over subsurface waters in polar regions. The average methylation rate over the Southern Ocean is relatively low (~0.05 $year^{-1}$) and comparable to rates found near the center of subtropical gyres. However, observed MeHg concentrations at 500-m depth in the Southern Ocean range between 400 and 600 fM (Figure 3f). High MeHg concentrations in the Southern Ocean are preserved by low temperatures that inhibit demethylation (0.090 $year^{-1}$, compared with 0.18 and 0.15 $year^{-1}$ in the Indian Ocean Gyre and tropical Pacific Ocean).

In a previous modeling study, Semeniuk and Dastoor (2017) proposed that the MeHg demethylation (k_m) rate is proportional to OCRR, which is similar to the Hg^{II} methylation rate (k_{dm}). At steady state,

$$\left[Hg^{II}\right]\times k_m\times \mathrm{OCRR} = [\mathrm{MeHg}]\times k_{dm}\times \mathrm{OCRR},$$

which results in MeHg concentrations that are proportional to concentrations of Hg^{II}:

$$[\mathrm{MeHg}] : \left[Hg^{II}\right] \equiv k_m : k_{dm}.$$

This reaction mechanism predicts a similar MeHg pattern in the thermocline as that of inorganic Hg^{II}. Namely, the lowest MeHg concentrations are modeled over the deep water formation region in the subarctic North Atlantic. Modeled concentrations are higher over the South Atlantic and the Southern Ocean due to an increase in water mass age following thermohaline circulation. The highest modeled concentrations are in the North Pacific Ocean with the oldest water mass ages (Semeniuk & Dastoor, 2017). This appears to be inconsistent with available observations in the subarctic Pacific Gyre (SHIPPO and P16N) and tropical Atlantic and Pacific Oceans (RITS) (Figures 2 and 3) and suggests OCRR is not an appropriate proxy for MeHg demethylation rates. The model of Semeniuk and Dastoor (2017) substantially underestimates high MeHg concentrations observed in the Southern Ocean, which the authors attribute to missing abiotic methylation processes or reduced Hg^{II} bioavailability associated with DOC and sea ice. Here we provide an alternative hypothesis that high MeHg concentrations are mainly caused by inhibition of demethylation at low temperatures.

3.2.6. A Unified Scheme

The association between MeHg concentrations and microbial activity has been widely alluded to in previous studies by correlations with NPP, OCRR, apparent oxygen utility, and nutrient concentrations (e.g., NO_3^- and PO_4^{3-}) across ocean regions (e.g., Kim et al., 2017; Munson et al., 2015; Sunderland et al., 2009). However, these relationships have typically only been developed at the basin scale. For instance, the relationship between OCRR and MeHg concentrations found in the North Pacific Ocean does not hold for the equatorial and South Pacific Oceans (Munson et al., 2015). In this study, we also account for other factors such as Hg^{II} substrate availability, solar radiation, and temperature and propose a unified scheme for MeHg formation and degradation for the global ocean that generates results consistent with available observations.

3.3. Global Budget

Figure 5 summarizes the modeled budget for MeHg over the global ocean. Overall, the modeled global total mass of MeHg in the ocean is 290 Mmol with 90 Mmol above 1,000-m depth. Our modeled MeHg mass is approximately two times higher than the budget derived by Semeniuk and Dastoor (2017) (160 Mmol). This difference is largely associated with high MeHg concentrations in polar regions and tropical regions. The modeled average fraction of MeHg over total Hg in the global total ocean (1,900 Mmol) is 15%. This fraction is highest over the 100–1,000-m depth (22%) and lowest over the surface ocean (11%). In the surface ocean, fast turnover between inorganic Hg species and MeHg due to active primary production and photochemical demethylation results in a short MeHg lifetime (21 days). Given a surface ocean current speed of

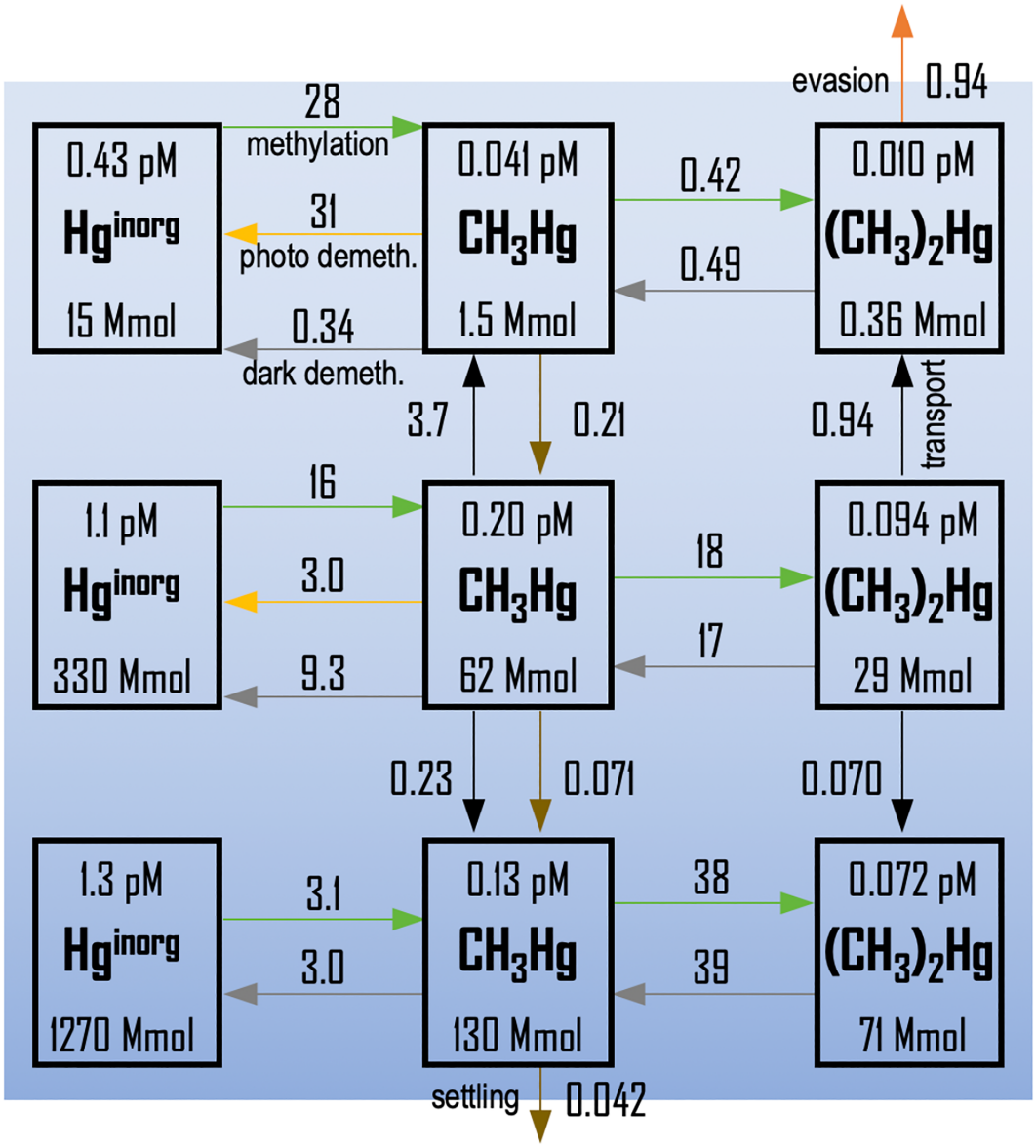

Figure 5. MeHg mass budget for the global ocean. The global ocean is divided into the top 100 m, 100–1,000 m, and below 1,000 m, respectively. Numbers on top of tracer names are average concentrations while those below are total masses. Numbers near arrows are mass flows in units of Mmol/year. Green and yellow arrows between inorganic Hg, CH_3Hg, and $(CH_3)_2Hg$ indicate biological methylation and photodemethylation, respectively. Gray arrows denote dark (biotic/abiotic) demethylation. Black arrows between layers indicate physical transport (advection and diffusion). The orange arrow out of the top of box is for $(CH_3)_2Hg$ evasion to the atmosphere, and the brown ones are for sinking fluxes with particulate organic matter.

approximately 1–10 cm s^{-1} (Feely et al., 2006), the transport of MeHg is 20–200 km before it is degraded. This indicates that the spatial pattern of MeHg in the surface ocean is largely controlled by local production and degradation rates without effective long-range transport. The lifetime of MeHg is longer in the subsurface and deep oceans because of the absence of photodemethylation: 7.4 and 67 years, respectively. This means that isopycnal and diapycnal transport are more significant processes influencing the MeHg distribution at these depths. Indeed, the observations are generally smoother and with less small-scale variability in subsurface waters compared to the surface ocean (Figure 2a). Relatively short lifetimes mean MeHg maintains a dynamic equilibrium with inorganic Hg species in the top 1,000 m of the water column. The total MeHg mass in the global ocean is increasing slowly at a rate of 0.02 Mmol/year. This increase is

caused by net inorganic Hg inputs to the ocean driven by anthropogenic Hg releases (Streets et al., 2019; Zhang, Jaeglé, Thompson, & Streets, 2014). There is also a net increase in MeHg mass below 1,000-m depth range (0.35 Mmol/year) driven by the downward diffusion fluxes from above.

The model indicates a net upward transport flux of MeHg (4.7 Mmol/year) from the subsurface ocean to the top 100 m. This is driven by the large vertical MeHg concentration gradient near the bottom of the euphotic layer, which has been observed globally in vertical measurements of MeHg (Table 2; Figure 3). Besides fast demethylation, evasion of $(CH_3)_2Hg$ to the atmosphere (0.94 Mmol/year) contributes to relatively low MeHg concentrations in the surface ocean. Despite the lower MeHg concentrations, the model budget shows that the surface ocean produces more MeHg than the upper ocean (100–1,000 m). This is counterintuitive but can be explained by fast photodemethylation in the surface ocean that lowers the MeHg concentrations. Such fast methylation rates were observed by Lehnherr et al. (2011) in the Arctic Ocean waters as well. Overall, the upward diffusion flux is 17% of in situ methylation in the surface layer with regional variations (8% at tropical Pacific Ocean and 36% for the Southern Ocean; Figure 5).

In the deep ocean below 1,000 m, both methylation and demethylation are much slower due to reduced microbial activity and low temperatures. The magnitude and spatial patterns of MeHg concentrations are instead influenced by physical transport and particle sinking. Burial of MeHg in deep ocean sediment (0.042 Mmol/year) is a minor term for the global mass budget. The transformation between CH_3Hg and $(CH_3)_2Hg$ is less constrained than that between Hg^{II} and MeHg due to a lack of observation. Many cruises report summed MeHg concentrations instead of CH_3Hg and $(CH_3)_2Hg$ separately. However, limited observations show that the ranges of $(CH_3)_2Hg$/MeHg are 3–20% in the upper ocean (Munson et al., 2015; Bowman et al., 2015), and the CH_3Hg: $(CH_3)_2Hg$ ratio is about 2 throughout much of the subsurface water column at the SAFe station (Hammerschmidt & Bowman, 2012). Our model results agree with these observations reasonably well with a global average ratio of CH_3Hg to $(CH_3)_2Hg$ of 1.8.

3.4. CH_3Hg Bioaccumulation

Figure 6a shows the modeled average CH_3Hg in all phytoplankton types per wet weight (wet wt) in the global ocean (0–100 m). In panels b–g, the contributions of the six different types of phytoplankton to the total CH_3Hg mass in phytoplankton cells are also shown. The global average CH_3Hg concentration in phytoplankton is ~2.0 ng/g wet wt. The spatial pattern of CH_3Hg in phytoplankton generally follows that of seawater CH_3Hg because a fast equilibrium is assumed across the cell membrane.

High-modeled phytoplankton CH_3Hg concentrations in polar regions (2–6 ng/g wet wt) are driven by high seawater CH_3Hg concentrations (Figure 2a). However, in the tropical Pacific Ocean, where seawater CH_3Hg concentrations are generally low due to fast photodemethylation, phytoplankton CH_3Hg concentrations are similar or higher than in the polar regions (4–8 ng/g wet wt). This reflects the dominance of prochlorococcus in tropical regions. Prochlorococcus has a large surface area to volume ratio (diameter = 0.6 μm), which facilitates CH_3Hg uptake (Figure 6e). The VCF for prochlorococcus is 20 times higher than for diatoms (d = 12 μm) (Table 1), which are abundant in the Southern Ocean and Pacific Subarctic Gyre. Differences in phytoplankton community composition offset the positive effect of lower CH_3Hg concentrations in tropical regions. One exception is the equatorial ocean where large eukaryotic diatoms dominate due to relatively high nutrient concentrations. Nevertheless, in this area, the upwelling of CH_3Hg-rich water from the subsurface ocean compensates the low VCF values of these large phytoplankton (Figure 2a).

Synechococcus also has a large surface area to volume ratio (d = 1.8 μm) and thus effectively bioaccumulate CH_3Hg from seawater. Phytoplankton in this size fraction are widely distributed between the Arctic and the center of North/South Atlantic/Pacific Gyres. Other phytoplankton types (including other large, trichodesmium, and coccolithophores) play a less important role. DOC variability seems to be unimportant for most regions due to the narrow concentration range (~40–80 μM) in the global open ocean, which translates to an ~30% change in VCF values. This contrasts the dominant role of terrestrial DOC for CH_3Hg uptake observed in coastal and shelf environments (Schartup et al., 2018).

Overall, our model suggests that global average phytoplankton CH_3Hg concentrations exhibit a relatively narrow concentration range between 1.2–3.6 ng/g wet wt, which is consistent with observations in the central Pacific (0.1–4 ng/g) (Gosnell & Mason, 2015). In the western North Atlantic coastal region, the observed

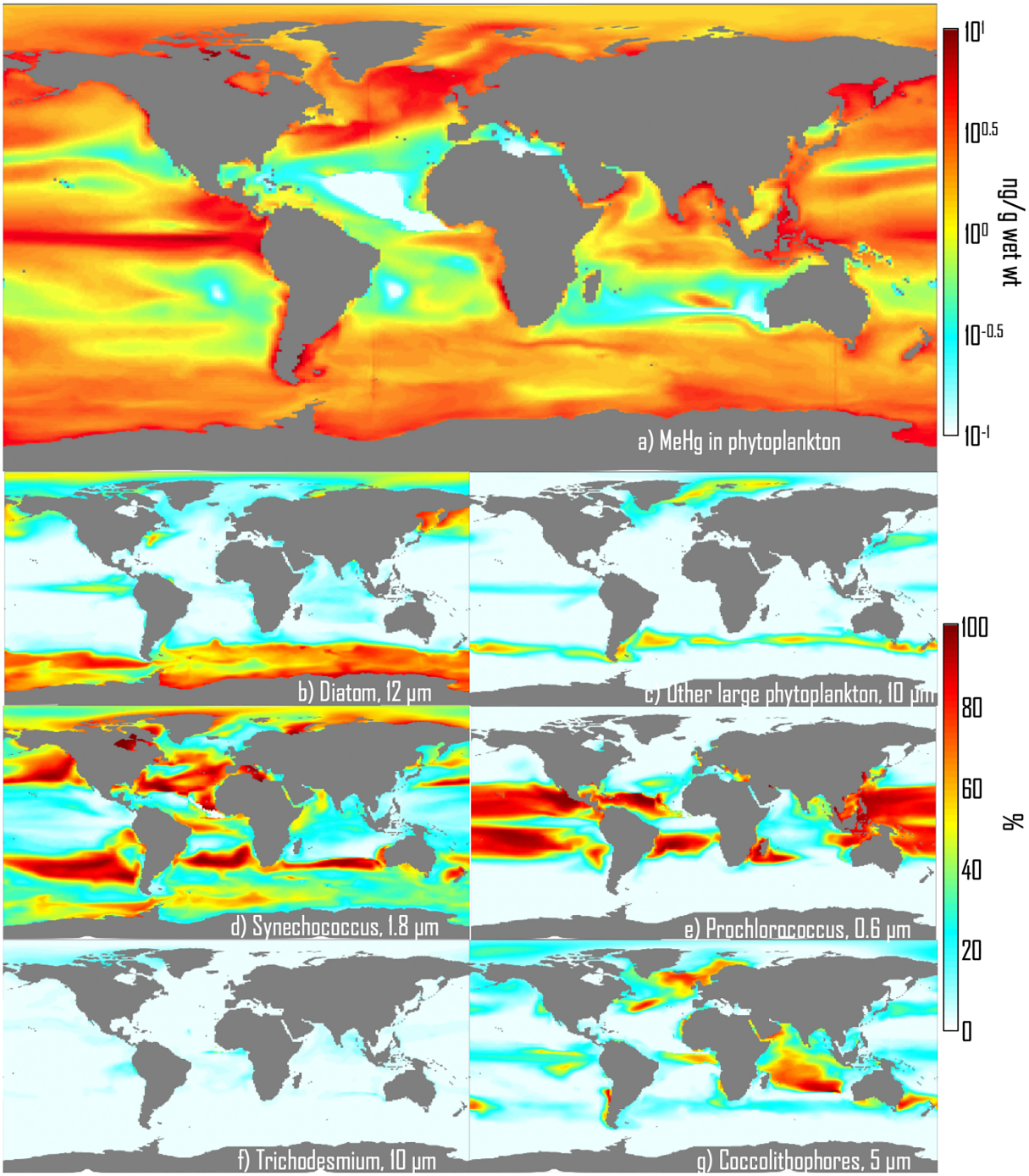

Figure 6. CH_3Hg concentrations in phytoplankton. (a) Average concentrations in all phytoplankton (ng CH_3Hg/g wet weight); (b–g) fractions of CH_3Hg in different phytoplankton for (b) diatoms, (c) other large phytoplankton, (d) synechococcus, (e) prochlorococcus, (f) trichodesmium, and (g) coccolithophores.

concentrations are, however, lower than the modeled values (0.01–0.5 ng/g wet wt (Schartup et al., 2018)). Most coastal data are from environments with higher and terrestrial-derived DOC values (110–150 µM) than the open ocean, which results in up to a factor 2 and 3 lower VCF values and subsequently lower CH_3Hg concentrations in the phytoplankton. Our model cannot reproduce these coastal observations due to the coarse resolution and lack of terrestrial sources of DOC. Previous work has suggested cell growth could reduce the phytoplankton CH_3Hg concentrations per unit biomass due to biodilution in productive systems (Hammerschmidt et al., 2013; Lee & Fisher, 2016; Mason et al., 1996). Here, the focus of our

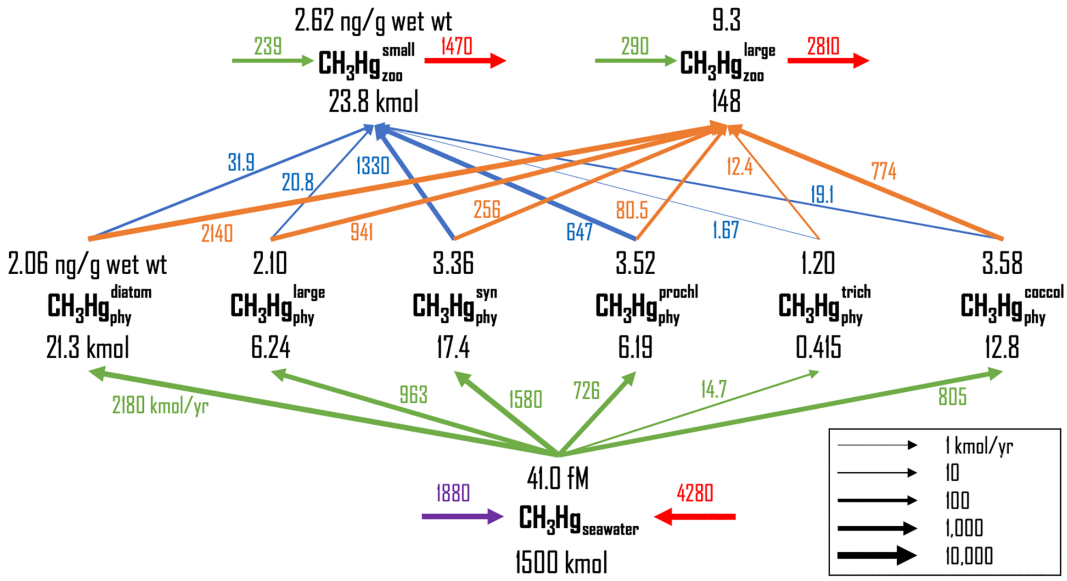

Figure 7. Planktonic food web dynamics for CH_3Hg in the global ocean. CH_3Hg concentrations per wet weight of plankton cells in units of ng/g wet weight are shown above each species, and the total mass of CH_3Hg in these cells in kmol are shown below. The six categories of phytoplankton include diatoms, large (other large phytoplankton), prochl (prochlorococcus), syn (synechococcus), trich (trichodesmium), and coccol (coccolithophores). The blue and orange arrows indicate trophic transfer to small and large zooplankton, respectively. The green arrows show MeHg uptake from seawater to plankton. The red arrows indicate release of CH_3Hg from zooplankton after death, and the purple arrow pointing to the bottom CH_3Hg symbol represents the flux of unassimilated MeHg returned to seawater. The width of these arrows is proportional to the logarithm of the magnitudes of the fluxes.

analysis is the annual mean CH_3Hg concentrations in phytoplankton. A sensitivity run shows that its impact on annual mean CH_3Hg concentrations in phytoplankton is fairly small, as this effect is dampened by the temporal averaging of the model (Figure S5).

3.5. CH_3Hg in Zooplankton

An instantaneous equilibrium is assumed for CH_3Hg between seawater and phytoplankton cells in the model. The flux into the marine food web is thus driven by loss, that is, grazing by herbivorous zooplankton. Figure 7 shows the CH_3Hg flow along the marine plankton food web. Variability in the dietary preference of phytoplankton by zooplankton means that small zooplankton mainly feed on picoplankton, with 96% of CH_3Hg from prochlorococcus and synechococcus. Similarly, large zooplankton receives CH_3Hg mainly from diatoms, coccolithophores, and other large phytoplankton (92%). Overall, diatoms and synechococcus are the two most important phytoplankton categories for transferring CH_3Hg from seawater to zooplankton, contributing 35% and 25%, respectively. Other large phytoplankton, coccolithophores and prochlorococcus, contributes to the remaining 40%. Because of the low dietary preference of trichodesmium by both zooplankton size classes and its low biomass (Dutkiewicz et al., 2009), the CH_3Hg trophic transfer via these phytoplankton is small (<0.2%).

Zooplankton CH_3Hg concentrations in the two size categories are mainly influenced by the CH_3Hg concentrations in their food sources (Figure 8). CH_3Hg concentrations in large zooplankton are highest (>10 ng/g wet wt) over the Southern Ocean, Pacific Subarctic Gyre, Equatorial Ocean, and the subarctic Atlantic, where large phytoplankton such as diatoms and coccolithophores dominate. Zooplankton CH_3Hg concentrations are much lower (0.1–0.3 ng/g wet wt) over the low-latitude and subtropical regions, where picoplankton dominates. The spatial pattern of CH_3Hg concentrations in small zooplankton is distinct from that of the large zooplankton, with high concentrations in the tropical ocean and Northern Hemispheric high-latitude oceans, where prochlorococcus and synechococcus dominate.

Overall, larger zooplanktons have higher CH_3Hg concentration (9.3 ng/g wet wt) than small zooplankton (2.6 ng/g wet wt). This partially reflects lower elimination rates from the larger zooplankton (a factor of ~2;

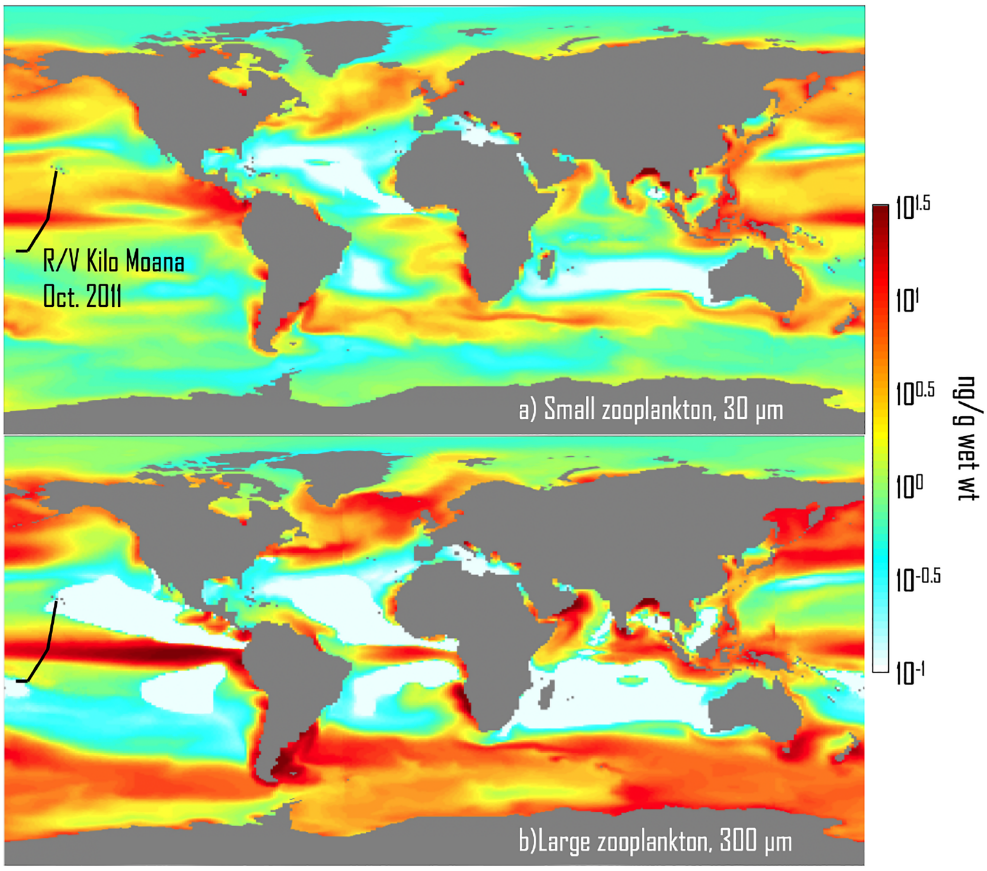

Figure 8. CH_3Hg concentrations in herbivorous zooplankton. (a) Small (diameter = 30 μm) and (b) large (diameter = 300 μm). The cruise track of Gosnell and Mason (2015) is also shown.

Table 1). Slower elimination than dietary intake results in bioaccumulation of CH_3Hg in larger zooplankton (Hammerschmidt & Fitzgerald, 2006). On the other hand, small zooplankton have lower CH_3Hg concentrations than their main prey (i.e., prochlorococcus and synechococcus) due to fast elimination. The modeled influence of temperature on the CH_3Hg elimination rate is small with a 14% difference across a temperature range of 0–20 °C.

Similar to marine phytoplankton, observations of CH_3Hg concentrations in pelagic marine zooplankton remain scarce, but the model results are within the range of observations in the open ocean (1.7–2.8 ng/g wet wt; Hirota et al., 1979, 1989). Gosnell and Mason (2015) reported zooplankton MeHg concentration along a cruise from Honolulu, Hawaii to Apia, Samoa in the central Pacific Ocean (cruise track is shown in Figure 8). They found a concentration range of 0.2–3.4 ng/g wet wt for different latitudes and size classes of plankton. The highest concentrations are observed over the upwelling region near the equator but decrease by a factor of 2 and 3 over higher latitudes. Our modeled spatial pattern is consistent with these observations (Figure 8).

3.6. CH_3Hg Biomagnification

The trophic magnification factor (TMF) is calculated as the ratio between the average CH_3Hg concentrations in all zooplankton and the average CH_3Hg concentrations in all phytoplankton at a given location (both in the units of ng/g wet wt). Model result shows that CH_3Hg biomagnifies in the marine plankton food web and predicts a global average TMF of 3.4 between phytoplankton and zooplankton (Figure 9), consistent with observed values (2.3–10) (Hammerschmidt & Fitzgerald, 2006; Kehrig et al., 2010; Kim et al., 2006, 2008). The spatial distribution of this TMF is largely driven by variability in zooplankton CH_3Hg concentrations because phytoplankton CH_3Hg concentrations have a relatively narrow range in the global ocean

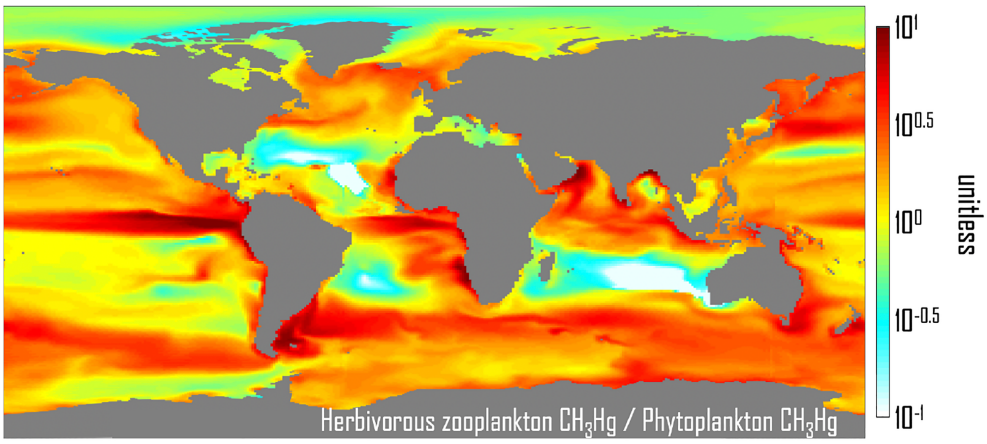

Figure 9. Trophic magnification factor (defined as the ratio of concentrations) for CH_3Hg between herbivorous zooplankton and phytoplankton.

(Figure 6a). By contrast, for coastal ecosystems Schartup et al. (2018) found that phytoplankton concentrations were highly variable due to large differences in environmental factors (DOC, productivity, and CH_3Hg), but the competing influences of growth dilution and dietary intake in zooplankton dampened such differences.

Two major food chains can be identified from the CH_3Hg trophic transfer flux as indicated by Figure 7: from synechococcus/prochlorococcus to small zooplankton and from diatoms/other large phytoplankton/coccolithophores to large zooplankton. In both food chains, species at lower trophic levels are the major prey for predators. TMF values range from 0.74–0.78 for the first food chain (i.e., no biomagnification) and 2.6–4.5 for the second one.

The highest modeled TMF (7.7) is observed in the eastern tropical Pacific Ocean (especially in the equatorial region). This TMF is associated with the internal grazing in the zooplankton pool, which effectively elongates the marine food web (i.e., carnivorous zooplankton) (Dutkiewicz et al., 2009). Internal grazing rate is proportional to the quadratic of zooplankton biomass. Thus, biomagnification is most prominent in productive regions such as the equatorial region and upwelling zones along the edge of the eastern boundary currents (Figure 9). Other productive regions such as the Southern Ocean and subarctic Atlantic Ocean have TMF values of 1.8 and 2.2, respectively. By contrast, TMF values are close to or even less than 1 over the subtropical and Arctic regions, where the smallest sizes of phytoplankton and zooplankton dominate (Figure 6). Overall, our model predicts that TMF values are generally higher over regions dominated by large-size zooplankton and slower elimination/mortality. These regions are also the biogeoprovinces where the largest phytoplankton species dominate.

3.7. Potential Impacts of Global Change

MeHg formation and trophic transfer are sensitive to ocean biogeochemistry. Changing ocean biogeochemistry due to climate driven changes is expected to have a large impact on marine MeHg formation and bioaccumulation (Krabbenhoft & Sunderland, 2013). Future ocean scenarios indicate a shallower carbon remineralization depth due to warmer seawater temperatures. This may shift MeHg formation to shallower depths, where it undergoes rapid photodemethylation but may be more likely to enter productive epipelagic food webs. Increasing seawater temperatures in a future ocean may also accelerate the degradation of MeHg.

Warmer seawater temperatures and lower seawater pH (ocean acidification) in the future is expected to alter the distribution and community structure of phytoplankton, which will eventually impact MeHg bioaccumulation and biomagnification. Lower seawater pH may alter the competitive fitness between phytoplankton types and significantly change the community structure (Dutkiewicz et al., 2015). The fraction of small phytoplankton is likely to increase due to lower nutrients concentrations (Dutkiewicz et al., 2013). Diatoms will find less favorable conditions as enhanced opal (SiO_2) export from the euphotic layer resulting from

faster OCRR (Segschneider & Bendtsen, 2013). Changes are likely to be most prominent over the polar and equatorial regions. However, additional studies are needed to identify positive and negative feedbacks among these processes. The model developed here provides an ideal quantitative framework for such detailed future studies.

Acknowledgments
The authors acknowledge financial support from the U.S. National Science Foundation (OCE 1260464). We thank Stephanie Dutkiewicz from MIT and Mike Long from Harvard University for **their** help **in** setting up the model. All the model and data are available at http://ebmg.online/data.html.

References

Agather, A. M., Bowman, K. L., Lamborg, C. H., & Hammerschmidt, C. R. (2019). Distribution of mercury species in the western Arctic Ocean (U.S. GEOTRACES GN01). *Marine Chemistry*, *216*, 103686.

Amos, H. M., Jacob, D. J., Streets, D. G., & Sunderland, E. M. (2013). Legacy impacts of all-time anthropogenic emissions on the global mercury cycle. *Global Biogeochemical Cycles*, *27*(2), 410–421.

Balcom, P. H., Hammerschmidt, C. R., Fitzgerald, W. F., Lamborg, C. H., & O'Connor, J. S. (2008). Seasonal distributions and cycling of mercury and methylmercury in the waters of New York/New Jersey harbor estuary. *Marine Chemistry*, *109*, 1–17.

Black, F. J., Poulin, B. A., & Flegal, A. R. (2012). Factors controlling the abiotic photo-degradation of monomethylmercury in surface waters. *Geochimica et Cosmochimica Acta*, *84*, 492–507.

Bowman, K. L., Eric Collins, R., Agather, A. M., Lamborg, C. H., Hammerschmidt, C. R., Kaul, D., et al. (2019). Distribution of mercury-cycling genes in the Arctic and equatorial Pacific Oceans and their relationship to mercury speciation. *Limnology and Oceanography*, *9999*, 1–11.

Bowman, K. L., Hammerschmidt, C. R., Lamborg, C. H., & Swarr, G. (2015). Deep-sea Research II Mercury in the North Atlantic Ocean: The U. S. GEOTRACES zonal and meridional sections. *Deep Sea Research Part II: Topical Studies in Oceanography*, *116*, 251–261.

Bowman, K. L., Hammerschmidt, C. R., Lamborg, C. H., Swarr, G. J., & Agather, A. M. (2016). Distribution of mercury species across a zonal section of the eastern tropical South Pacific Ocean (U.S. GEOTRACES GP16). *Marine Chemistry*, *186*, 156–166.

Bratkič, A., Vahčič, M., Kotnik, J., Obu, K., Vazner, E., Begu, E., et al. (2016). Mercury presence and speciation in the South Atlantic Ocean along the 40°S transect. *Global Biogeochemical Cycles*, *30*, 105–119.

Brown, N. L., Stoyanov, J. V., Kidd, S. P., & Hobman, J. L. (2003). The MerR family of transcriptional regulators. *FEMS Microbiology Reviews*, *27*(2-3), 145–163. https://doi.org/10.1016/S0168-6445(03)00051-2

Canário, J., Santos-Echeandia, J., Padeiro, A., Amaro, E., Strass, V., Klaas, C., et al. (2017). Mercury and methylmercury in the Atlantic sector of the Southern Ocean. *Deep Sea Research Part II: Topical Studies in Oceanography*, *138*, 52–62.

Cossa, D., Averty, B., & Pirrone, N. (2009). The origin of methylmercury in open Mediterranean waters. *Limnology and Oceanography*, *54*(3), 837–844.

Cossa, D., Heimbürger, L.-E., Lannuzel, D., Rintoul, S. R., Butler, E. C. V., Bowie, A. R., et al. (2011). Mercury in the Southern Ocean. *Geochimica et Cosmochimica Acta*, *75*(14), 4037–4052.

DiMento, B. P., & Mason, R. P. (2017). Factors Controlling the Photochemical Degradation of Methylmercury in Coastal and Oceanic Waters. *Marine Chemistry*, *196*, 116–125. https://doi.org/10.1016/j.marchem.2017.08.006

Dutkiewicz, S., Follows, M. J., & Bragg, J. G. (2009). Modeling the coupling of ocean ecology and biogeochemistry. *Global Biogeochemical Cycles*, *23*(4), GB4017. https://doi.org/10.1029/2008gb003405

Dutkiewicz, S., Morris, J. J., Follows, M. J., Scott, J., Levitan, O., Dyhrman, S. T., & Berman-Frank, I. (2015). Impact of ocean acidification on the structure of future phytoplankton communities. *Nature Climate Change*, *5*(11), 1002–1006.

Dutkiewicz, S., Scott, J. R., & Follows, M. J. (2013). Winners and losers: Ecological and biogeochemical changes in a warming ocean. *Global Biogeochemical Cycles*, *27*(2), 463–477.

Feely, R., Sabine, C., Millero, F., Wanninkhof, R., & Hansell, D. (2006). Carbon dioxide, hydrographic, and chemical data obtained during the R/V Thomas Thompson cruise in the Pacific Ocean on CLIVAR repeat hydrography sections P16N_2006 (Feb. 14–Mar. 30, 2006), Report, Carbon Dioxide Inf. Anal. Cent., Oak Ridge Natl. Lab., Oak Ridge, Tenn.

Fitzgerald, W. F., Lamborg, C., & Hammerschmidt, C. (2007). Marine biogeochemical cycling of mercury. *Chemical Reviews*, *107*, 641–662.

Forget, G., Campin, J. M., Heimbach, P., Hill, C. N., Ponte, R. M., & Wunsch, C. (2015). ECCO version 4: An integrated framework for non-linear inverse modeling and global ocean state estimation. *Geoscientific Model Development*, *8*(10), 3071–3104.

Fu, X., Feng, X., Zhang, G., Xu, W., Li, X., Yao, H., et al. (2010). Mercury in the marine boundary layer and seawater of the South China Sea: Concentrations, sea/air flux, and implication for land outflow. *Journal of Geophysical Research*, *115*, D06303. https://doi.org/10.1029/2009JD012958

Gionfriddo, C. M., Tate, M. T., Wick, R. R., Schultz, M. B., Zemla, A., Thelen, M. P., et al. (2016). Microbial mercury methylation in Antarctic sea ice. *Nature Microbiology*, *1*(10), 16127. https://doi.org/10.1038/nmicrobiol.2016.127

Gosnell, K. J., & Mason, R. P. (2015). Mercury and methylmercury incidence and bioaccumulation in plankton from the central Pacific Ocean. *Marine Chemistry*, *177*, 772–780.

Hammerschmidt, C. R., & Bowman, K. L. (2012). Vertical methylmercury distribution in the subtropical North Pacific Ocean. *Marine Chemistry*, *132-133*, 77–82.

Hammerschmidt, C. R., Finiguerra, M. B., Weller, R. L., & Fitzgerald, W. F. (2013). Methylmercury accumulation in plankton on the continental margin of the northwest Atlantic Ocean. *Environmental Science & Technology*, *47*(8), 3671–3677. https://doi.org/10.1021/es3048619

Hammerschmidt, C. R., & Fitzgerald, W. F. (2006). Bioaccumulation and trophic transfer of methylmercury in Long Island Sound. *Archives of Environmental Contamination and Toxicology*, *51*(3), 416–424.

Hammerschmidt, C. R., Fitzgerald, W. F., Lamborg, C. H., Balcom, P. H., & Visscher, P. T. (2004). Biogeochemistry of methylmercury in sediments of Long Island Sound. *Marine Chemistry*, *90*(1-4), 31–52.

Hansell, D. A., Carlson, C. A., Repeta, D. J., & Schlitzer, R. (2009). Dissolved organic matter in the ocean: A controversy stimulates new insights. *Oceanography*, *22*(4), 202–211.

Heimburger, L. E., Sonke, J. E., Cossa, D., Point, D., Lagane, C., Laffont, L., et al. (2015). Shallow methylmercury production in the marginal sea ice zone of the central Arctic Ocean. *Scientific Reports*, *5*, 1–6.

Heyes, A., Mason, R., Kim, E., & Sunderland, E. (2006). Mercury methylation in estuaries: Insights from using measuring rates using stable mercury isotopes. *Marine Chemistry*, *102*(1-2), 134–147.

Hirota, R., Fujiki, M., & Tajima, S. (1979). Mercury contents of zooplankton collected in the tropical Pacific Ocean. *Bull. Japan. Soc. Sci. Fish*, *45*, 1449–1451.

Hirota, R., Fukuda, Y., Chiba, J., Tajima, S., & Fujiki, M. (1989). Mercury content of copepods (crustacean) collected from the Antarctic Sea. *Proc. NIPR Symp. Polar Biol.*, *2*, 65–70.

Hollweg, T. A., Gilmour, C. C., & Mason, R. P. (2009). Methylmercury production in sediments of Chesapeake Bay and the mid-Atlantic continental margin. *Marine Chemistry*, *114*(3-4), 86–101.

Horowitz, H. M., Jacob, D. J., Amos, H. M., Streets, D. G., & Sunderland, E. M. (2014). Historical Mercury releases from commercial products: Global environmental implications. *Environmental Science & Technology*, *48*(17), 10242–10250.

Horowitz, H. M., Jacob, D. J., Zhang, Y., Dibble, T. S., Slemr, F., Amos, H. M., et al. (2017). A new mechanism for atmospheric mercury redox chemistry: Implications for the global mercury budget. *Atmospheric Chemistry and Physics*, *17*(10), 6353–6371.

Kehrig, H. A., Seixas, T. G., Baeta, A. P., Malm, O., & Moreira, I. (2010). Inorganic and methylmercury: Do they transfer along a tropical coastal food web? *Marine Pollution Bulletin*, *60*(12), 2350–2356. https://doi.org/10.1016/j.marpolbul.2010.08.010

Kim, E., Mason, R. P., & Bergeron, C. M. (2008). A modeling study on methylmercury bioaccumulation and its controlling factors. *Ecological Modelling*, *218*(3-4), 267–289.

Kim, E. H., Mason, R. P., Porter, E. T., & Soulen, H. L. (2006). The impact of resuspension on sediment mercury dynamics, and methylmercury production and fate: A mesocosm study. *Marine Chemistry*, *102*(3-4), 300–315.

Kim, H., Soerensen, A. L., Hur, J., Heimbürger, L.-E., Hahm, D., Rhee, T. S., et al. (2017). Methylmercury mass budgets and distribution characteristics in the western Pacific Ocean. *Environmental Science & Technology*, *51*(3), 1186–1194. https://doi.org/10.1021/acs.est.6b04238

Kim, H., Van Duong, H., Kim, E., Lee, B. G., & Han, S. (2014). Effects of phytoplankton cell size and chloride concentration on the bioaccumulation of methylmercury in marine phytoplankton. *Environmental Toxicology*, *29*(8), 936–941. https://doi.org/10.1002/tox.21821

Kirk, J. L., Louis, V. L. S., Hintelmann, H., Lehnherr, I., Else, B., & Poissant, L. (2008). Methylated mercury species in marine waters of the Canadian high and sub Arctic. *Environmental Science & Technology*, *42*(22), 8367–8373. https://doi.org/10.1021/es801635m

Krabbenhoft, D. P., & Sunderland, E. M. (2013). Environmental science. *Global change and mercury, Science*, *341*(6153), 1457–1458. https://doi.org/10.1126/science.1242838

Kuss, J., Zülicke, C., Pohl, C., & Schneider, B. (2011). Atlantic mercury emission determined from continuous analysis of the elemental mercury sea-air concentration difference within transects between 50°N and 50°S. *Global Biogeochemical Cycles*, *25*, n/a. https://doi.org/10.1029/2010GB003998

Lamborg, C. H., Hammerschmidt, C. R., & Bowman, K. L. (2016). An Examination of the Role of Particles in Oceanic Mercury Cycling. *Philosophical Transanction of the Royal Society a Mathematical Physical and Engineering Science*, *374*(2081). https://doi.org/10.1098/rsta.2015.0297

Lee, C.-S., & Fisher, N. S. (2016). Methylmercury uptake by diverse marine phytoplankton. *Limnology and Oceanography*, *61*(5), 1626–1639. https://doi.org/10.1002/lno.10318

Lehnherr, I., Louis, V. L. S., Hintelmann, H., & Kirk, J. L. (2011). Methylation of inorganic mercury in polar marine waters. *Nature Geoscience*, *4*, 298–302.

Mahaffey, K. R., Sunderland, E. M., Chan, H. M., Choi, A. L., Grandjean, P., Mariën, K., et al. (2011). Balancing the benefits of n-3 polyunsaturated fatty acids and the risks of methylmercury exposure from fish consumption. *Nutrition Reviews*, *69*(9), 493–508. https://doi.org/10.1111/j.1753-4887.2011.00415.x

Marshall, J., Adcroft, A., Hill, C., Perelman, L., & Heisey, C. (1997). A finite-volume, incompressible Navier Stokes model for studies of the ocean on parallel computers. *Journal of Geophysical Research*, *102*(C3), 5753–5766.

Mason, R., & Fitzgerald, W. F. (1993). The distribution and biogeochemical cycling of mercury in the equatorial Pacific Ocean. *Deep Sea Research, Part I*, *40*(9), 1897–1924.

Mason, R. P., Choi, A. L., Fitzgerald, W. F., Hammerschmidt, C. R., Lamborg, C. H., Soerensen, A. L., & Sunderland, E. M. (2012). Mercury biogeochemical cycling in the ocean and policy implications. *Environmental Research*, *119*, 101–117. https://doi.org/10.1016/j.envres.2012.03.013

Mason, R. P., Reinfelder, J. R., & Morel, F. M. M. (1996). Uptake, toxicity, and trophic transfer of mercury in a coastal diatom. *Environmental Science & Technology*, *30*, 1835–1845.

Mason, R. P., & Sullivan, K. A. (1999). The distribution and speciation of mercury in the South and equatorial Atlantic. *Deep-Sea Research Part II-Topical Studies in Oceanography*, *46*(5), 937–956.

Matilainen, T., & Verta, M. (1995). Mercury methylation and demethylation in aerobic surface waters. *Canadian Journal of Fisheries and Aquatic Sciences*, *52*, 1597–1608.

Matsumoto, K., Honda, M. C., Sasaoka, K., Wakita, M., Kawakami, H., & Watanabe, S. (2014). Seasonal variability of primary production and phytoplankton biomass in the western Pacific subarctic gyre: Control by light availability within the mixed layer. *Journal of Geophysical Research: Oceans*, *119*, 6523–6534.

Monperrus, M., Tessier, E., Amouroux, D., Leynaert, A., Huonnic, P., & Donard, O. F. X. (2007). Mercury methylation, demethylation and reduction rates in coastal and marine surface waters of the Mediterranean Sea. *Marine Chemistry*, *107*(1), 49–63.

Motta, L. C., Blum, J. D., Johnson, M. W., Umhau, B. P., Popp, B., Washburn, S. J., et al. (2019). Mercury cycling in the North Pacific Subtropical Gyre as revealed by mercury stable isotope ratios. *Global Biogeochemical Cycles*, *33*(6), 777–794. https://doi.org/10.1029/2018GB006057

Munson, K. M., Lamborg, C. H., Boiteau, R. M., & Saito, M. A. (2018). Dynamic mercury methylation and demethylation in oligotrophic marine water. *Biogeosciences*, *15*, 6451–6460.

Munson, K. M., Lamborg, C. H., Swarr, G. J., & Saito, M. A. (2015). Mercury species concentrations and fluxes in the central tropical Pacific Ocean. *Global Biogeochemical Cycles*, *29*(5), 656–676.

Nightingale, P. D., Malin, G., Law, C. S., Watson, A. J., Liss, P. S., Liddicoat, M. I., et al. (2000). In situ evaluation of air-sea gas exchange parameterizations using novel conservative and volatile tracers. *Global Biogeochemical Cycles*, *14*(1), 373–387.

Parks, J. M., Johs, A., Podar, M., Bridou, R., Hurt, R. A. Jr., Smith, S. D., et al. (2013). The genetic basis for bacterial mercury methylation. *Science*, *339*(6125), 1332–1335. https://doi.org/10.1126/science.1230667

Pickhardt, P. C., & Fisher, N. S. (2007). Accumulation of inorganic and methylmercury by freshwater phytoplankton in two contrasting water bodies. *Environmental Science & Technology*, *41*(1), 125–131. https://doi.org/10.1021/es060966w

Podar, M., Gilmour, C. C., Brandt, C. C., Soren, A., Brown, S. D., Crable, B. R., et al. (2015). Global prevalence and distribution of genes and microorganisms involved in mercury methylation. *Science Advances*, *1*, 1–13.

Schaefer, J. K., Yagi, J., Reinfelder, J. R., Cardona, T., Ellickson, K. M., Tel-Or, S., & Barkay, T. (2004). Role of the bacterial organomercury lyase (MerB) in controlling methylmercury accumulation in mercury-contaminated natural waters. *Environmental Science & Technology*, *38*(16), 4304–4311. https://doi.org/10.1021/es049895w

Schartup, A. T., Balcom, P. H., Soerensen, A. L., Gosnell, K. J., Calder, R. S. D., Mason, R. P., & Sunderland, E. M. (2015). Freshwater discharges drive high levels of methylmercury in Arctic marine biota. *Proceedings of the National Academy of Sciences of the United States of America*, *112*(38), 11,789–11,794. https://doi.org/10.1073/pnas.1505541112

Schartup, A. T., Ndu, U., Balcom, P. H., Mason, R. P., & Sunderland, E. M. (2015). Contrasting effects of marine and terrestrially derived dissolved organic matter on mercury speciation and bioavailability in seawater. *Environmental Science & Technology*, *49*(10), 5965–5972. https://doi.org/10.1021/es506274x

Schartup, A. T., Qureshi, A., Dassuncao, C., Thackray, C. P., Harding, G., & Sunderland, E. M. (2018). A model for methylmercury uptake and trophic transfer by marine plankton. *Environmental Science & Technology*, *52*(2), 654–662. https://doi.org/10.1021/acs.est.7b03821

Segschneider, J., & Bendtsen, J. (2013). Temperature-dependent remineralization in a warming ocean increases surface pCO2 through changes in marine ecosystem composition. *Global Biogeochemical Cycles*, *27*(4), 1214–1225.

Semeniuk, K., & Dastoor, A. (2017). Development of a global ocean mercury model with a methylation cycle: Outstanding issues. *Global Biogeochemical Cycles*, *31*, 400–433.

Soerensen, A. L., Jacob, D. J., Schartup, A. T., Fisher, J. A., Lehnherr, I., Louis, V. L. S., et al. (2016). A mass budget for mercury and methylmercury in the Arctic Ocean. *Global Biogeochemical Cycles*, *30*(4), 560–575.

Soerensen, A. L., Mason, R. P., Balcom, P. H., Jacob, D. J., Zhang, Y., Kuss, J., & Sunderland, E. M. (2014). Elemental mercury concentrations and fluxes in the tropical atmosphere and ocean. *Environmental Science & Technology*, *48*(19), 11,312–11,319.

Soerensen, A. L., Schartup, A. T., Skrobonja, A., Bouchet, S., & Amouroux, D. (2018). Deciphering the role of water column redoxclines on methylmercury cycling using speciation modeling and observations from the Baltic Sea. *Global Biogeochemical Cycles*, *32*, 1498–1513.

Soerensen, A. L., Sunderland, E. M., Holmes, C. D., Jacob, D. J., Yantosca, R. M., Skov, H., et al. (2010). An improved global model for air-sea exchange of mercury: High concentrations over the North Atlantic. *Environmental Science & Technology*, *44*(22), 8574–8580. https://doi.org/10.1021/es102032g

Streets, D. G., Horowitz, H. M., Jacob, D. J., Lu, Z., Levin, L., Ter Schure, A. F. H., & Sunderland, E. M. (2017). Total mercury released to the environment by human activities. *Environmental Science & Technology*, *51*(11), 5969–5977. https://doi.org/10.1021/acs.est.7b00451

Streets, D. G., Horowitz, H. M., Lu, Z., Levin, L., Thackray, C. P., & Sunderland, E. M. (2019). Five hundred years of anthropogenic mercury: Spatial and temporal release profiles. *Environmental Research Letters*, *14*(8), 084004. https://doi.org/10.1088/1748-9326/ab281f

Sunderland, E. M., Gobas, F. A. P. C., Heyes, A., Branfireun, B., Bayer, A., Cranston, R., & Parsons, M. (2004). Speciation and bioavailability of mercury in well-mixed estuarine sediments. *Marine Chemistry*, *90*, 91–105.

Sunderland, E. M., Krabbenhoft, D. P., Moreau, J. W., Strode, S. A., & Landing, W. M. (2009). Mercury sources, distribution, and bioavailability in the North Pacific Ocean: Insights from data and models. *Global Biogeochemical Cycles*, *23*, GB2010. https://doi.org/10.1029/2008GB003425

Sunderland, E. M., Li, M., & Bullard, K. (2018). Decadal changes in the edible supply of seafood and methylmercury exposure in the United States. *Environmental Health Perspectives*, *126*(1), 017006. https://doi.org/10.1289/EHP2644

Sunderland, E. M., & Mason, R. P. (2007). Human impacts on open ocean mercury concentrations. *Global Biogeochemical Cycles*, *21*, GB4022. https://doi.org/10.1029/2006GB002876

Ward, B. A., Dutkiewicz, S., & Follows, M. J. (2013). Modelling spatial and temporal patterns in size-structured marine plankton communities: Top-down and bottom-up controls. *Journal of Plankton Research*, *36*(1), 31–47.

Whalin, L., Kim, E.-H., & Mason, R. (2007). Factors influencing the oxidation, reduction, methylation and demethylation of mercury species in coastal waters. *Marine Chemistry*, *107*(3), 278–294.

Wozniak, B., & Dera, J. (2007). *Light absorption in sea water* (Vol. 2007, p. 463). New York: Springer Science, Business Media.

Zhang, Y., Horowitz, H., Wang, J., Xie, Z., Kuss, J., & Soerensen, A. L. (2019). A coupled global atmosphere-ocean model for air-sea exchange of mercury: Insights into wet deposition and atmospheric redox chemistry. *Environmental Science & Technology*, *53*(9), 5052–5061. https://doi.org/10.1021/acs.est.8b06205

Zhang, Y., Jacob, D. J., Dutkiewicz, S., Amos, H. M., Long, M. S., & Sunderland, E. M. (2015). Biogeochemical drivers of the fate of riverine mercury discharged to the global and Arctic oceans. *Global Biogeochemical Cycles*, *29*(6), 854–864.

Zhang, Y., Jaeglé, L., & Thompson, L. (2014). Natural biogeochemical cycle of mercury in a global three-dimensional ocean tracer model. *Global Biogeochemical Cycles*, *28*(5), 553–570.

Zhang, Y., Jaeglé, L., Thompson, L., & Streets, D. G. (2014). Six centuries of changing oceanic mercury. *Global Biogeochemical Cycles*, *28*(11), 1251–1261.